



CENTRO DE INVESTIGACIONES EN ÓPTICA A.C.

**Synthesis and characterization of ZnO and
YAG:Ce³⁺,Pr³⁺ nanophosphors for white light
generation by photoluminescence and
electroluminescence.**

THESIS SUBMITTED IN PARTIAL FULFILLMENT OF THE
REQUIREMENTS FOR THE DEGREE OF DOCTOR OF
SCIENCE(OPTICS) AT CENTRO DE INVESTIGACIONES EN
OPTICA

Msc. JORGE ROBERTO OLIVA UC

For the Degree of

Doctor of Science (Optics)

León Guanajuato, México

January 2014

**Advisor: Dr. Elder de la Rosa Cruz,
Co-Advisor: Dr. Luis Armando Diaz-Torres.**

FINAL VERSION

Research Advisors:

Dr. Elder de la Rosa Cruz

(DEPARTMENT OF PHOTONICS, CIO)

Dr. Luis Armando Díaz-Torres

(DEPARTMENT OF PHOTONICS, CIO)

Reviewers:

Dr. Ramon Carriles Jaimes

(DEPARTMENT OF PHOTONICS, CIO)

Dr. Enrique Castro Camus

(DEPARTMENT OF PHOTONICS, CIO)

Dr. Efrain Mejia Beltran

(DEPARTMENT OF PHOTONICS, CIO)

Dr. Alejandro Torres Castro

(DEPARTMENT OF MATERIALS, CIIDIT-FIME UANL)

Acknowledgments

First of All, I would like to thank my Advisor Dr. Elder de la Rosa for his courage and support to finish my work of PhD. He showed me how to be a critical person and a good scientist.

To my Co-Advisor Luis Diaz-Torres for his invaluable time to explain me about physics of materials.

To Dr. Anvar Zakhidov for receiving me in UTD and develop my research about HyLEDs, his kindness was important for me, also he encouraged me to work hardly. In addition, I have to thank Alexios Papadimitratos because he is a great teacher for OLEDs and he taught me how to work in laboratory correctly, and Kamil for his suggestions about how to solve some problems presented during my stay in UTD.

I have to be grateful with all my friends in the nanophotonics and advanced materials group, Leonardo, Isaac, Tzarara, Haggeo. They accompanied me almost all time in difficult moments and they helped me to go ahead with my work of thesis.

To my mother and father, they are simply the reason for which I want to progress in life. They showed me that we have to jump big rocks to be a great person.

Abstract

In this dissertation two materials Zinc Oxide (ZnO) and Yttrium aluminum garnet doped with rare earths (YAG:Ce³⁺,Pr³⁺) were studied to efficiently emit blue, yellow or white light. The route of chemical synthesis permitted us to choose the type of defect associated to certain color of emission in ZnO and YAG nanophosphors, while the work of engineering employed using such materials, allowed us to fabricate electroluminescent devices for applications in illumination. In the case of ZnO, the type of defects was tailored by using Triethanolamine (TEA) or dodecylamine (DCA) as surfactants. ZnO nanoparticles with an average size of 5nm, emitted blue light and yellow light centered at 429 nm and 580 nm when they were synthesized with TEA and dispersed in hexane. By using DCA as surfactant, the ratio between the blue and yellow emission bands in ZnO was controlled, that in turn, permitted us to tune the photoluminescence from cool to warm white light. In addition, ZnO based LEDs using ZnO nanoparticles synthesized with DCA were fabricated, and white light electroluminescence with coordinates of (0.31, 0.33) according to the international commission on illumination (CIE) was obtained. The turn on voltage for those devices was 4V and the maximum current consumption for the LEDs was 2.32 mA at 10V.

The structural and luminescent properties of Y₃Al₅O₁₂/Y₄Al₂O₉:Ce³⁺(0.1%)-Pr³⁺(0.1%) nanophosphors synthesized by a simple hydrothermal method were also studied. The Ammonia introduced during synthesis increased the

stabilization of YAG from 55 wt% to 63 wt% in the samples annealed at 900⁰C, in consequence, an increment of 83% of the overall emission in those phosphors under 460 nm excitation was observed. Moreover, some samples presented a broad red emission band (due to the presence of Cr impurities) overlapped to the green-yellow emission of Ce³⁺ excited under 340 nm. By taking advantage of this broad green-yellow-red emission and using a blue dye, white light photoluminescence with CIE coordinates of (0.30, 0.36) was produced. Finally, hybrid LEDs were fabricated employing YAG:Ce³⁺ nanophosphors, those had a maximum brightness of 266 Cd/m² at 9V. All These results demonstrate that the method of synthesis and configuration for hybrid LEDs could be useful for the development of lighting sources and displays.

Contents

Chapter 1: A general Overview

1.0 Introduction.....	8
1.1 ZnO nanocrystals, applications and types of defects for emission...	8
1.2 YAG doped with rare earths and applications.....	10
1.3 State of the art in solid state lighting.....	11
1.4 Theory of Polymer light emitting diodes.....	12
1.4.1 Electroluminescence and PLED structure.....	13
1.4.2 Device Operation.....	15
1.4.3 Photometric quantities.....	17
1.4.4 EL efficiencies.....	18
1.5 Hybrid LEDs.....	19
<i>References for chapter 1.....</i>	<i>20</i>

Chapter 2: Experimental Methods for Characterization of Nanoparticles and Hybrid LEDs.

2.0 Introduction.....	24
2.1 Morphology Characterization.....	24
2.1.1 Transmission electron microscopy (TEM) method.....	24
2.1.2 Scanning Electron Microscopy (SEM) method.....	25
2.2 Structural Characterization.....	26
2.2.1 XRD pattern.....	26
2.2.2 Raman spectra.....	28
2.3 Optical characterization.....	29
2.3.1 Absorption measurements.....	29
2.3.2 Fluorescence measurements.....	29
2.3.3 Infra-Red Fourier Spectroscopy (FTIR).....	30
2.4 Characterization of the Hybrid LEDs.....	31
<i>References for chapter 2.....</i>	<i>32</i>

Chapter 3: White Light Generation from ZnO Nanoparticles by Photoluminescence and Electroluminescence

3.0 Introduction.....	33
3.1 Synthesis of ZnO nanoparticles and characterization.....	33
3.1.1 Synthesis of ZnO.....	33

3.1.2 Structural, morphological and optical characterization.....	35
3.1.3 Effect of TEA on the Structure and Morphology of ZnO quantum dots.....	35
3.1.4 Effect of TEA on the Absorption and Band Gap of ZnO quantum dots.....	40
3.1.5 The Role of TEA on the Impurities.....	42
3.2 Photoluminescence measurements.....	43
3.2.1 Blue Emission and Origin of Defects Produced by TEA.....	43
3.2.2 Effect of TEA on the Luminescence of ZnO quantum dots.....	48
3.2.3 Quantum Yield.....	50
3.2.4 Yellow Emission.....	51
3.3 White Light Emission.....	55
3.4 Schematic for defects emitting blue and yellow light.....	58
3.5 ZnO based LEDs for white light generation.....	61
3.6 Conclusions for chapter 3.....	65
<i>References Chapter 3.....</i>	66

Chapter 4: White Light generation from YAG: Ce³⁺ and YAG/YAM: Ce³⁺,Pr³⁺,Cr³⁺ Nanophosphors by Photoluminescence and Electroluminescence

4.0 Introduction.....	69
4.1 Synthesis of YAG/YAM:Ce ³⁺ and YAG/YAM:Ce ³⁺ ,Pr ³⁺ ,Cr ³⁺ nanophosphors and characterization.....	69
4.1.1 Blue dye-impregnating procedure.....	71
4.1.2 Structural and morphological characterization.....	72
4.2 Impurities.....	75
4.3 Optical Properties.....	77
4.3.1 The fluorescent properties of YAG/YAM:Ce ³⁺ ,Pr ³⁺ ,Cr ³⁺ under 460 nm excitation.....	77
4.3.2 The fluorescent properties of YAG/YAM:Ce ³⁺ ,Pr ³⁺ ,Cr ³⁺ under 340 nm excitation.....	82
4.4 White light emission under 340 nm excitation.....	85
4.5 Hybrid LEDs made with YAG:Ce ³⁺ nanophosphors.....	87
4.6 Conclusions for chapter 4.....	91
<i>References chapter 4.....</i>	93

Chapter 5: Conclusions

5.0 Conclusions	96
-----------------------	----

Chapter 1

A general Overview

1.0 Introduction

This chapter presents a general overview about synthesis and characterization of ZnO and YAG phosphors reported in the literature, as well as general concepts to understand the physics of Polymer Light emitting diodes (PLEDs).

1.1 ZnO nanocrystals, applications and types of defects for emission

ZnO nanocrystals have attracted the attention of many research groups due to their potential applications in different areas such as biological systems, optoelectronics, solar cells and sensing, to mention a few [1-4]. It is a direct bandgap semiconductor with a room temperature bandgap of 3.37 eV and a large excitonic (electron-hole) binding energy of 60 meV, larger than the thermal energy at room temperature (26 meV) [5]. This difference in the binding energy combined with an efficient excitonic recombination form the basis of room temperature lasing of ZnO [5]. Recently, UV lasing was reported with a threshold power density as low as 40 kW/cm² for a directional grown nanorod array, much lower than the threshold for polycrystalline powder and GaN with a binding energy of 25 meV [6]. The characteristic emission band of ZnO is centered at 390 nm and is attributed to free exciton recombination. Green (520 nm) and a broad orange (620 nm) emission bands have been reported in both nano- and bulk crystals. The former has been associated to the recombination of a photogenerated hole with the single ionized charge state of the single ionized oxygen vacancy on or very close to the surface of the particle, and the second band has been associated to excess of oxygen inside the particle [7,8]. Weak blue emission has been reported and ascribed to electron transition from shallow donor level of oxygen vacancies ($\Delta E_g = \sim 2.8$ eV) and zinc interstitial defects ($\Delta E_g = \sim 2.7$ eV) to the valence band [9, 10]. Both oxygen vacancies and then zinc

interstitial were probably formed during the synthesis process due to the kinetics parameters. Recently, strong blue emission was reported and suggested to arise from the formation of surface ZnO/oleic acid (OA) complexes formed when hydroxyl groups coming from DEA reacts with carboxyl groups from oleic acid [11]. Those visible bands make ZnO a very attractive low-voltage phosphor for field emission displays. All defects responsible for visible emission are produced during the synthesis process but, in general, are not fully controlled either in their presence or in their density. Furthermore, those defects can change from one batch to another one. Thus, controlling the synthesis process in order to select and control the presence of specific defects is a challenge, and is a very important subject of research around the world.

Several groups have been working to control size, morphology, photoluminescence (PL) and the energy band gap (BG); various surfactant and capping agents have been used, obtaining particles with sizes ranging from 10-25 nm and BG ~ 3.86 to 4 eV [12,13]. The use of oleic acid not only induces surface defects associated with blue emission but also controls the size and morphology of the nanocrystals [11]. More recently triethanolamine (TEA) has been used to control the size and morphology of ZnO nanoparticles, with sizes ranging from 3-75 nm and morphologies such as spheres, rugbyball-like, rice-like and nanorods as well as BG values from 3.27 to 3.94 eV. Those changes in shape are possible because TEA permits the formation of stable complexes such as $\text{Zn}(\text{OH})_2$ and $\text{Zn}(\text{OH})_4^{2-}$ which act as growth units [14,15]. Thus, TEA could be useful as capping agent in ZnO nanoparticles and as a modifier of morphology as demonstrated in this thesis. It could be more advantageous to use TEA as surfactant to produce blue light instead of OA, because it needs to be combined with some compounds such as DEA to form carboxylate groups on the surface of ZnO nanocrystals which in turn create defects for blue emission [11]. In this thesis, only TEA was used to produce defects associated with blue light; thus reducing the cost of synthesis. In addition,

TEA along with changes in the temperature of synthesis, produced yellow light emitting defects.

1.2 YAG doped with rare earths and applications

Trivalent cerium doped YAG phosphors ($\text{Y}_3\text{Al}_5\text{O}_{12}:\text{Ce}^{3+}$) have demonstrated its reliability for applications in discharge lamps and phosphor converted light emitting Diodes (pc-LEDs) to produce white light [1-2, 16,17]. However, the commercial $\text{YAG}:\text{Ce}^{3+}$ based LEDs present a low color rendering index ($\text{CRI}<80$) because the red component is poor. Some research groups have been working to incorporate this red component as well as to reach the optimal CIE (Commission Internationale d'Eclairage) coordinates of (0.33,0.33) by codoping with rare earth (RE) the $\text{YAG}:\text{Ce}^{3+}$ nanophosphors. Several ions have been used for this purpose, Gd^{3+} induces a small shift of yellow emission toward longer wavelength, while Eu^{3+} , Sm^{3+} , Pr^{3+} , Tb^{3+} produce a weak red emission after excitation at 470 nm [3-4, 18,19]. The CRI was improved to 80 by using Tb^{3+} , and 83 by using Pr^{3+} and annealing at temperature of 1500 °C [5-7 20-22]. For Pr^{3+} , the red emission was the result of energy transfer from Ce^{3+} (donor) to Pr^{3+} (acceptor) taking advantage that the acceptor has its $^3\text{P}_0$ levels in resonance with the $5d$ levels of Cerium [7, 22]. However, strong red emission of Pr^{3+} has been reported in hosts such as BaMoO_4 and CaTiO_3 by direct excitation at 450 nm and 330 nm respectively [8-9, 23,24]. Optimization of red emission has also been explored by modifying the synthesis process, solid-state reaction, combustion method and polyol method, drying procedure and annealing temperature [22-24]. Some problems derived from those procedures are the high temperatures of synthesis as well as the weak red contribution to $\text{YAG}:\text{Ce}^{3+}$ emission.

In order to overcome those problems and to improve red emission, $\text{YAG}:\text{Ce}^{3+},\text{Pr}^{3+}$ nanophosphos were synthesized by using the well-known hydrothermal process which also permits low cost and large scale production [10-11, 25,26]. To the best of our knowledge, there are no studies about a broad

red emission band of Pr^{3+} overlapped on Ce^{3+} emission in $\text{YAG:Ce}^{3+},\text{Pr}^{3+}$ nanophosphors under 340 nm excitation, only a weak peak in the range of 608 nm to 611 nm has been observed under 460 nm excitation.

1.3 State of the art in solid state lighting (SSL)

Nowadays research groups are focusing their energies to create new lighting sources for the generation of white light. Those types of sources are used for illumination indoors and outdoors. Currently, light emitting diodes (LEDs), fluorescent lamps and incandescent lamps are mainly used for lighting applications. The performance of commercial LEDs is higher compared to that of fluorescent or incandescent lamps. LEDs can generate above 100 lumens per watt (lm/W), while fluorescent and incandescent lamps can generate just 60 lm/W and 12 lm/W respectively [27]. The main problem for those white light lighting sources is the poor contribution of the red component in white light. A good balance among blue, green and red colors is needed to create a perfect white light [28]. The LEDs in the current market produce white light in the following way: the blue light generated from a LED excites a phosphor located on top of it, some blue light is absorbed by the phosphors and is re-emitted as green-yellow light. The combination of blue light passing the layer of phosphor and the green-yellow light generated by the phosphor, produces white light, however the red component of this type of LED is poor. Figure 1.1 shows the LED chip which produces blue light and the YAG phosphor (green-yellow emitter) deposited on it [29]:

Commercial LED chip

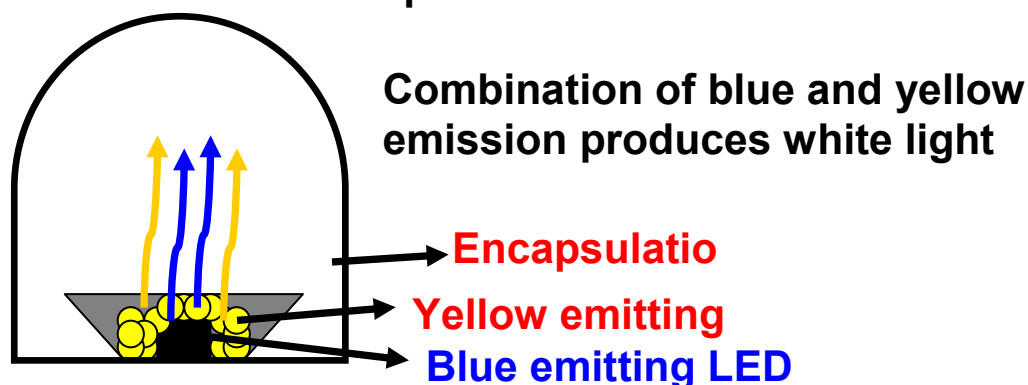


Figure 1.1: Basic design for a commercial LED.

The problem with the phosphor is the low quantum efficiency at about 56% [29]. This means that a blue photon does not generate a green or yellow photon. One way to eliminate this problem is using direct electroluminescent sources such as polymer light emitting diodes (PLEDs) [29]. Those PLEDs are interesting due to their applications in displays for cell phones, screens and lighting [30-32]. They can tune the white light emission from cool to warm white light and have an important red component. The light generated by PLEDs can surpass 150 lm/W. However, the problems with this type of lighting sources are cost of fabrication and lifetime [33]. To overcome those problems mentioned above, the development of hybrid lighting sources could be an option, since they can combine cheap materials (inorganic phosphors) with high efficient organic materials such as electroluminescent polymers. In this way the cost of fabrication is decreased and the efficiency maintained above 100 lm/W [34].

1.4 Theory of Polymer light emitting diodes

Some of the advantages for PLEDs are versatility to fabricate them on flexible substrates, tunability of color and compactness. Therefore, we decided to use them as a source of blue light, which in turn, will excite the nanophosphors synthesized in this work. We present briefly the physics of PLEDs in this section in order to understand the electrical and optical characteristics of the devices fabricated during this dissertation for the generation of white light.

1.4.1 Electroluminescence and PLED structure

The electroluminescence is defined as the generation of light by applying electric current. The PLED could be considered as a P-N junction, where the holes (p-part) are injected from the ITO anode passing the hole transport layers (HTL) toward the organic semiconductor (emitter) and electrons (n-part) are injected from a metal cathode passing the electron transport layers (ETL). The typical device structure of a PLED is shown in Fig. 1.2a,b where the emissive layer is sandwiched between two conductive electrodes. Figure 1.3a shows the energy band diagram of a typical orange light emitting diode: ITO/MEH-PPV/Al where ITO is indium tin oxide, MEH-PPV is Poly[2-methoxy-5-(2-ethylhexyloxy)-1,4-phenylenevinylene] and Al is aluminum. The energy band diagram is also presented under forward bias, see figure 1.3b. The transparency of ITO allows the light produced within the active layer to exit the device. The aluminum cathode which is a low function material (4.2 eV) is evaporated thermally. There are other options for low function materials: Mg (3.7 eV) or Ca (2.9 eV), those are widely used in the fabrication of OLEDs.

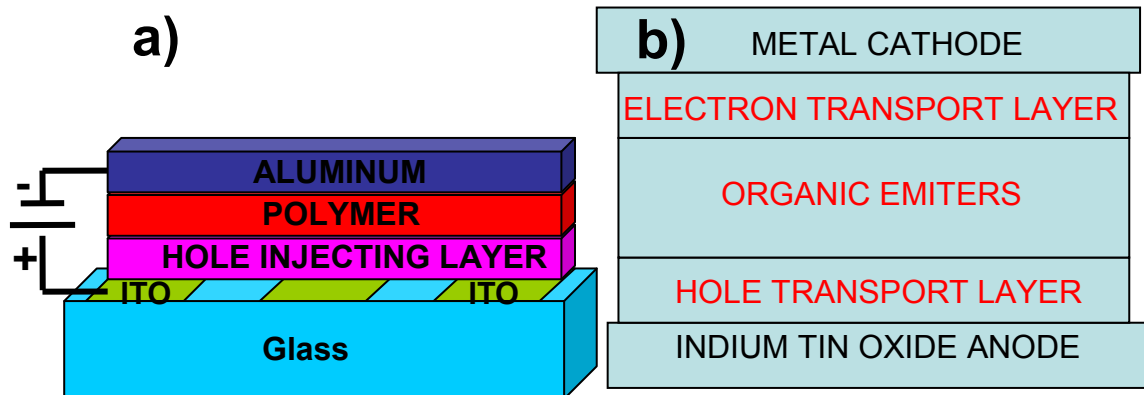


Figure 1.2 Device Structure of a PLED: a) basic structure, b) the structure of a multilayer device.

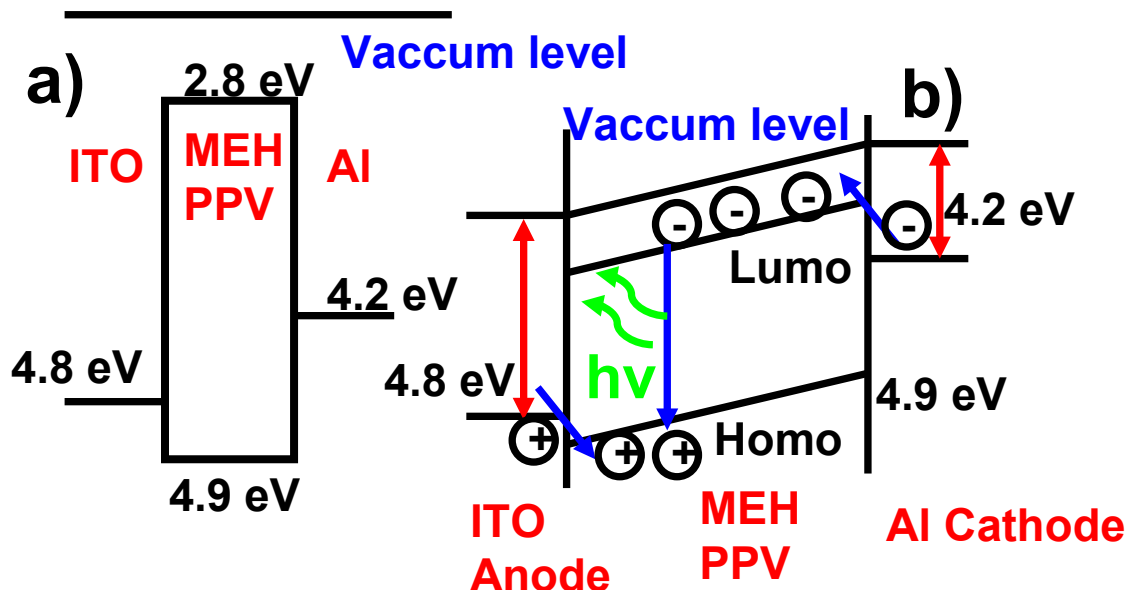


Figure 1.3: a) Energy position, relative to the vacuum level, of the frontier levels of the materials used in the device with a configuration of ITO/MEH-PPV/Al, b) band diagram for the same device under forward bias.

The emissive layer is a conjugated polymer with single and double carbon-carbon bonds. The single bond is called σ -bond, and the double bond is formed by a σ -bond and a π -bond [35]. The semiconducting properties of this type of polymer originate from the π -bond along the polymer chain. There are electrons in the π -bond which are loosely bound and those π electrons are the conduction electrons in conjugated polymers. The chemical structures of some conjugated polymers that are used as light emitting polymers (LEP) in PLED fabrication are shown in figure 1.4. All organic layer in PLEDs are deposited by spin coating, spin casting and the typical thicknesses are ranging from 10 to 100 nm. It is very important the roughness of those films, since it is directly related with the transport of charges, if the roughness is high, transport is difficult and then, the efficiency of recombination (exciton formation) is poor.

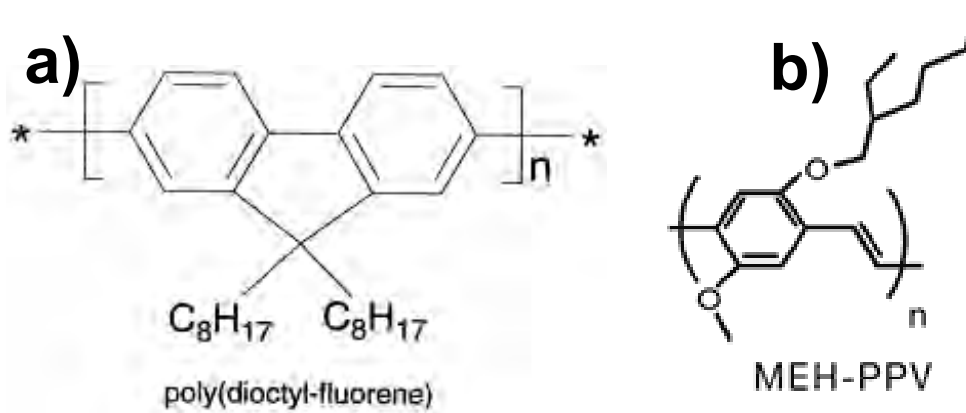


Figure 1.4: Chemical structures of some conjugated polymers that are used in electroluminescent diodes: a) Poly(9,9-dioctylfluorene) (PFO) and b) Poly [2-methoxy-5-(2-ethylhexyloxy)-1,4-phenylene vinylene] (MEH-PPV) [35].

1.4.2 Device Operation

The basic operation of a PLED consists in the injection of positive and negative charge carriers from the anode and cathode. Driven by the applied electric field, holes and electrons move through the polymer layers over a certain distance until they recombine with each other within the emitter to form excitons, then, the emission of light takes place as a result of radiative decay. Hence, PLED operation involves charge injection, charge transport, exciton formation and light emission, which is schematically illustrated in figure 1.3.

In the first step where charges are injected, there is a potential barrier for both, hole and electron from electrodes. The charge injection could be achieved by two mechanisms: Schottky thermal injection or Fowler-Nordheim tunneling injection. In Schottky mechanism, the current flow is described by:

$$j = \frac{4\pi qmk}{h^3} T^2 \exp\left(-\frac{q\Phi_{Bn}}{kT}\right) \left[\exp\left(\frac{qV}{kT}\right) - 1\right], \quad (1.1)$$

where m is the effective mass of the electron (hole), k is Boltzman's constant, h is the Planck's constant, T is temperature, q is the elementary charge, Φ_{Bn} is the barrier height, and V is the applied voltage [35]. In the Fowler-Nordheim tunneling mechanism, a charge carrier is injected with the assistance of a local high electric field (10^6 - 10^7 V/cm²) and the current flow is described by:

$$j = \frac{q^3 V^2 m_0}{8\pi h \Phi_{Bn} m^*} \exp\left(-\frac{4(2m^*)^{0.5} \Phi_{Bn}^{1.5}}{3h q V}\right), \quad (1.2)$$

where m_0 is the mass of the free electron and m^* is the effective mass [35].

After the holes and electrons are injected into the device, they are transported through the polymeric layers until they recombine in the electroluminescent polymer. The typical hole mobility is in the range of 10^{-7} - 10^{-3} cm²/Vs and the typical electron mobility is lower by a factor of 10-100 [35]. The low mobility in these materials results from the disorder in the amorphous or polycrystalline materials. This disparity in the mobility between holes and electrons makes difficult the choice of material to have good balance of recombination. This difference in mobility also permits an accumulation of the injected carriers near the polymer- electrode interface, but after a certain threshold of applied electric field, the carriers are moved into the electroluminescent layer. This threshold should be low to decrease the turn on voltage of the device. It is very important the rate of recombination for the efficiency of the device, ideally if each injected electron recombines with each injected hole (exciton formation), the internal quantum efficiency is 100%. However, the theoretical maximum external efficiency is just 40% [35].

1.4.3 Photometric quantities

It is important to know some preliminary concepts to understand the curves associated to the generation of light in PLEDs. Photometry is the science charged of measurement of light taking into account the human eye sensitivity. The measurement of no visible light is called radiometry. One essential unit for photometry is the lumen (or luminous flux), it refers to the total amount of light

emitted by a source taking into account the human's eye spectral luminous efficiency function $v(\lambda)$, according to this curve the maximum on sensitivity for human eye is located at 555 nm [35]. Another relevant concept is the luminous intensity (I_v), which is defined as the amount of light per unit solid angle in a certain direction:

$$I_v = \frac{d\Phi_v}{d\Omega} , \quad (1.3)$$

Where $d\Phi_v$ is the luminous flux going through the solid angle $d\Omega$ in a given direction. If the luminous intensity is divided by the area of the emitter or the reflecting surface, the Luminance (L_v) in Cd/m^2 is obtained. Table 1.1 summarizes the photometric units explained above:

Table 1.1:

Photometric quantity	Unit	Relationship with lumen
Luminous flux	Lm (lumen)	
Luminous intensity	Cd (candela)	Lm sr^{-1}
luminance	Cd m^{-2}	$\text{Lm sr}^{-1} \text{ m}^{-2}$

The emission of light from PLEDs is assumed to be Lambertian, that is, the brightness (Cd/m^2) is independent of the viewing angle. This is important for the characterization of PLEDs because the measurement of light is possible independent of the angle. Normally, light output is measured over a small solid angle in the forward direction, normal to the plane of the device [35].

1.4.4 EL efficiencies

One important parameter for the performance of PLEDs is efficiency. There are several efficiencies involved during the operation of an electroluminescent device:

a) External quantum efficiency (EQE): This efficiency is useful to calculate the amount of photon generated by each electron injected into the electroluminescent device.

b) Luminance Efficiency: This efficiency tell us the amount of luminous intensity generated by unit of current injected, it is given by [35]:

$$\Phi_{luminance} = \frac{L_v (Cd / m^2)}{J (A / cm^2)}, \quad (1.3)$$

Where L_v and J are the luminance and density of current of the electroluminescent device respectively.

c) Luminous Efficiency: This efficiency permit us to know the amount of light generated by the device in certain direction as a function of the electrical input. It is defined by [35]:

$$\Phi_{luminance} = \frac{\Phi_v}{IV}, \quad (1.4)$$

where IV is the electrical input power of the device.

The luminance efficiency and the luminous efficiency indicate us whether the consumption of current is high or not at certain level of brightness for practical applications. Typically, current is measured at 1000 C d/m² for applications in lighting.

1.5 Hybrid LEDs

PLEDs are suitable for compact lighting sources. The main problems for this type of technology are the degradation of the organic layers, due to the heating caused by the current passing through the device, and high cost of fabrication. They are also very sensitive to water and oxygen, those elements produce fast deterioration of PLEDs. Also, the packaging methods are difficult to use when PLEDs are fabricated on flexible substrates. Semiconductor nanocrystals (NCs) such as Quantum dots and oxides such as ZnO and YAG doped with rare earths, in contrast, are much more stable to degradation overtime in the presence of

oxygen and water than organic polymers used in PLEDs, making them very interesting as emitters in hybrid LEDs, which contains organic and inorganic materials. Those oxides are low cost materials, and therefore it would be interesting incorporating them in PLEDs. If the oxides mentioned above are efficient, they can be excited with the light generated from PLEDs. All those factors contributed to our motivation for the creation of hybrid light emitting devices, since they are promising to have properties of emission, lifetime and cost comparable to those presented in commercial lighting sources

References for chapter 1

- [1] R. Gopikrishnan, K. Zhang, P. Ravichandran, S. Baluchamy, V. Ramesh, S. Biradar, P. Ramesh, J. Pradhan, J. C. Hall, A. K. Pradhan, and G. T. Ramesh, Nano-Micro Letters 2, 31 (2010).
- [2] D. J. Rogers, F. H. Teherani, V. E. Sandana, and M. Razeghi, Proc. SPIE Vol. 7605, 76050 (2010).
- [3] Zeng Longyue, Dai Songyuan, Xu Weiwei, and Wang Kongjia, Plasma Sci. Technol. 8, 172 (2006).
- [4] J. Zhang, S. Wang., M. Xu, Y. Wang, B. Zhu, S. Zhang, W. Huang and S. Wu, Cryst. Growth Des. 9, 3532 (2009).
- [5] S. Mitsubori, I. Katayama, S.H. Lee, T. Yao and J . Takeda, J.phys.: condensed matter 21, 064211 (2009)
- [6] M.H. Huang, S. Mao, H. Feick, H. Yan, Y. Wu, H. Kind, E. Weber, R. Russo, and P. Yang, Science 292, 1897 (2001).
- [7] K. Vanheusden, W. L. Warren, C.H. Seager, D.R Tallant, J.A. Voigt, and B.E.J Gnade, J. Appl. Phys. 79, 7983 (1996).
- [8] J. W. P. Hsu, D. R. Tallant, R. L. Simpson, N. A. Missert, and R. G. Copeland, Appl. Phys. Lett 88, 252103 (2006).
- [9] G.H. Du, F. Xu, Z.Y. Yuan and G.V. Tendeloo, Appl. Phys. Lett 88, 243101 (2006).

- [10] D.H. Zhang, Z.Y. Xue and Q.P. Wang, J. Phys. D:Appl. Phys. 35, 2837 (2002).
- [11] Y.S. Fu, X.W. Du, S.A. Kulinich, J.S. Qiu, W.J. Qin, R. Li, J. Sun, and J. Liu, J. Am. Chem. Soc. 129, 16029 (2007).
- [12] N. Rajeswari Yogamalar, R. Srinivasan, and A. Chandra Bose, Opt. Mat. 31, 1570 (2009).
- [13] M.L. Singla, M. Shafeeq, and M. Manish Kumar, J. of Lumines. 129, 434 (2009).
- [14] L. Tang, B. Zhou, J. Zhao, X. Lv, F. Sun, and Z. Wang, Colloids and Surfaces A: Physicochem. Eng. Aspects 332, 43 (2009).
- [15] K. Thongsuriwong, P.Amornpitoksuk, and S.Suwanboon, J. of Phys. and Chem. of Solids 71, 730 (2010).
- [16] T. Mah, T. A. Parthasarathy, and H. D. Lee, Journal of Ceramic Processing Research. 5, 369 (2004).
- [17] H. S. Jang, Y. H. Won, and D. Y. Jeon, Appl. Phys. B 95, 715 (2009).
- [18] R. Mueller-Mach, G. O. Mueller, M. R. Krames, and T. Trottier, IEEE J. of selected topics in Quant. Electr. 8, 339 (2002).
- [19] Y. Pan, M. Wu, and Q. Su, J. of Phys. and Chem. of Solids 65, 845 (2004).
- [20] J. W. Lee, J. H. Lee, E. J. Woo, H. Ahn, J. S. Kim, and C. H. Lee, Ind. Eng. Chem. Res. 47, 5994 (2008).

- [21] H. S. Jang, W. B. Im, D. C. Lee, D. Y. Jeon, and S. S. Kim, J. of Lumin. 126, 371 (2007).
- [22] H. Yang, and Y. S. Kim, J. of Lumin. 128, 1570 (2008).
- [23] X. Yang, J. Liu, H. Yang, X. Yu, Y. Guo, Y. Zhou, and J. Liu, J. Mater. Chem. 19, 3771 (2009).
- [24] X. Zhang, J. Zhang, X. Zhang, L. Chen, Y. Luo, and X. J. Wang, Chem. Phys. Letters 434, 237 (2007).
- [25] Y. Zhang, and H. Yu, Ceramics International 35, 2077 (2009).
- [26] H. Yang, L. Yuan, G. Zhu, A. Yu, and H. Xu, Materials Letters 63, 2271 (2009).
- [27] C. C. Hsieh, Analysis of LED Technologies for Solid State Lighting Markets, Master's degree report, University of California, Berkeley 2012.
- [28] <http://energy.sandia.gov/?tag=solid-state-lighting&paged=6>
- [29] http://www.merck-performance-materials.com/en/lighting/led_function/led_function.html
- [30] F. Huang , H. Wu, and Y. Cao, Chem. Soc. Rev. 39, 2500 (2010).
- [31] J. Liu, Y. Shi, and Y. Yang, Appl. Phys. Lett. 79, 578 (2001).
- [32] H. J. Bolink, E. Coronado, J. Orozco, and M. Sessolo, Adv. Mater. 21, 79 (2009).

[33] J.H. Jou, Y. Qiu, S. Grigalevicius and E. Baranoff, Adv. In Mat. Sci. and Engin. 2012, 878301 (2012)

[34] [http://www.oled-info.com/lg/udc white oled technology exceeds 100 lm w](http://www.oled-info.com/lg/udc_white_oled_technology_exceeds_100_lm_w)

[35] Polymer light emitting diodes based on pol yfluorenes (author: Qiushu Zhang). Lambert Academic Publishing.

Chapter 2

Experimental Methods For characterization of nanoparticles and Hybrid LEDs

2.0 Introduction

In this chapter the techniques and methods to characterize the ZnO nanoparticles and doped YAG nanophosphors are presented.

2.1 Morphology Characterization

2.1.1 Transmission electron microscopy method

In transmission electron microscopy (TEM), a Gun made of lanthanum hexaboride (LaB_6) generate electrons, which are accelerated by high voltage (100-1000 kV) to a velocity approaching the speed of light (0.6-0.9 c). The associated wavelength is five orders of magnitude smaller than the light wavelength (0.04-0.008 Å) [1]. Figure 2.1a shows a typical setup for a TEM microscope. The electron beam is then focused by using magnetic lenses called condenser lenses, after this, a thin and focused beam is obtained. This beam hits some specific part in the sample and a part of electron passes through it. The transmitted beam is again focused using a system of lenses called objective lens, and an image is formed. This image is enlarged through the projector lenses according to the set magnification. Later this image is projected on a phosphor, that in turn, produces light and the user is able to visualize the image of the sample. In this image, darker areas represent the thicker regions of the sample, this is due to the poor transmission of electrons, the brighter areas represent thinner regions (more electrons were transmitted). This method permits us to see nanoparticles with sizes below 100 nm and crystalline planes. It is worthy to notice that the magnetic lens introduces aberrations such as coma and astigmatism and those ones are corrected using specialized software.

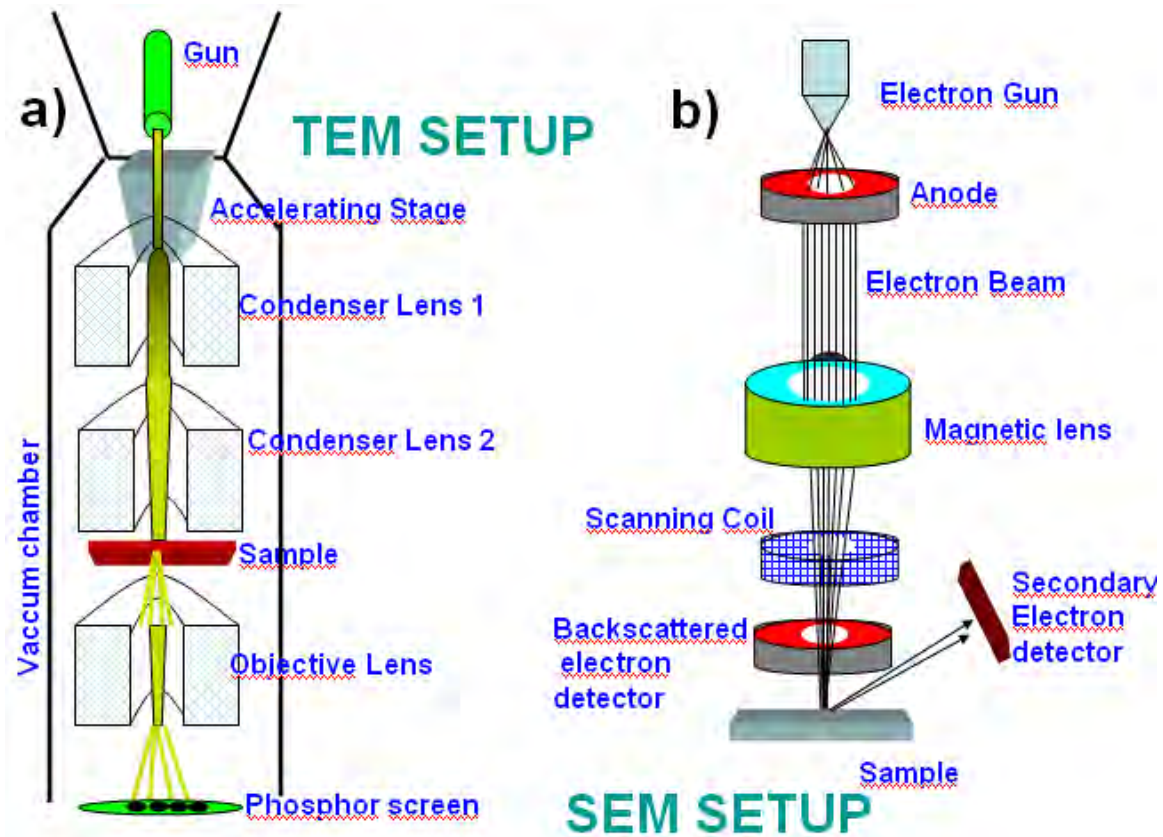


Figure 2.1 TEM and SEM setup

2.1.2 Scanning Electron Microscopy method

In Scanning Electron Microscopy (SEM), electrons are generated from a tungsten filament which acts as a cathode. This is heated up by applying a voltage. After this, the electrons are accelerated toward the anode which is the positive part with voltages in the range of 1-50 KV. The electron beam is focused on a very fine point in the sample by using magnetic lenses. During this process, the beam also passes through pairs of scanning coils, which create a magnetic field able to deflect the beam horizontally and vertically in such a way that the surface of the sample can be scanned. When the primary electron coming from the beam interacts with the volume of the sample, electrons lose energy by scattering and absorption. Those ones can penetrate up to 5 μm into the surface of the sample. The energy exchange between the electron beam and the sample produces the emission of electrons and electromagnetic radiation (X-rays), which

can be detected to produce an image. The detection of X-rays is useful for the chemical characterization of the sample, in this way, it is possible to know the composition of the sample from basic elements, and this method is called energy dispersive X-ray spectroscopy (EDX). The interaction of the incident beam with the sample can produce secondary electron and backscattered electrons, figure 2.1b shows the position of detector for each type of electron. Both, secondary or backscattered electrons can be used to obtain an image of the sample; however the spatial resolution is higher when secondary electrons are used to generate an image.

2.2 Structural Characterization

2.2.1 XRD pattern

The X-ray diffraction (XRD) is a useful technique to see X-ray scattering from crystalline materials. The XRD pattern is a fingerprint of these materials; therefore it is possible to identify the composition of organic or inorganic materials, interplanar distances and crystalline orientation. When an incident X-ray beam hits (at an angle θ) a crystalline arrangement containing atoms in certain positions (plane 1), the electromagnetic wave is partially reflected at an angle θ (the angle of incidence is equal to the angle of reflection), see figure 2.2a. If the reflection from the second plane is considered, the two reflected waves with the same phase will interfere constructively and a diffraction pattern will be observed. The condition for constructive interference of reflected waves from adjacent planes which are separated by distance d is given by the Bragg's Law:

$$n\lambda = 2d\sin\theta, \quad (2.1)$$

where n is a positive integer representing the order of reflection, λ is the wavelength of the incident x-ray. The diffracted angle, 2θ , is defined between the incident beam and the detection angle, see figure 2.2b. By using x-ray detectors, it is possible to know the intensity of the reflected x-rays, such intensity and the

position of diffraction peaks are associated to unique lattice planes in the crystal structure. In a diffraction pattern, the maximum intensity has a value of 100 and the rest of peaks are scaled relative to that value. Hence, each peak represents a family of lattice planes.

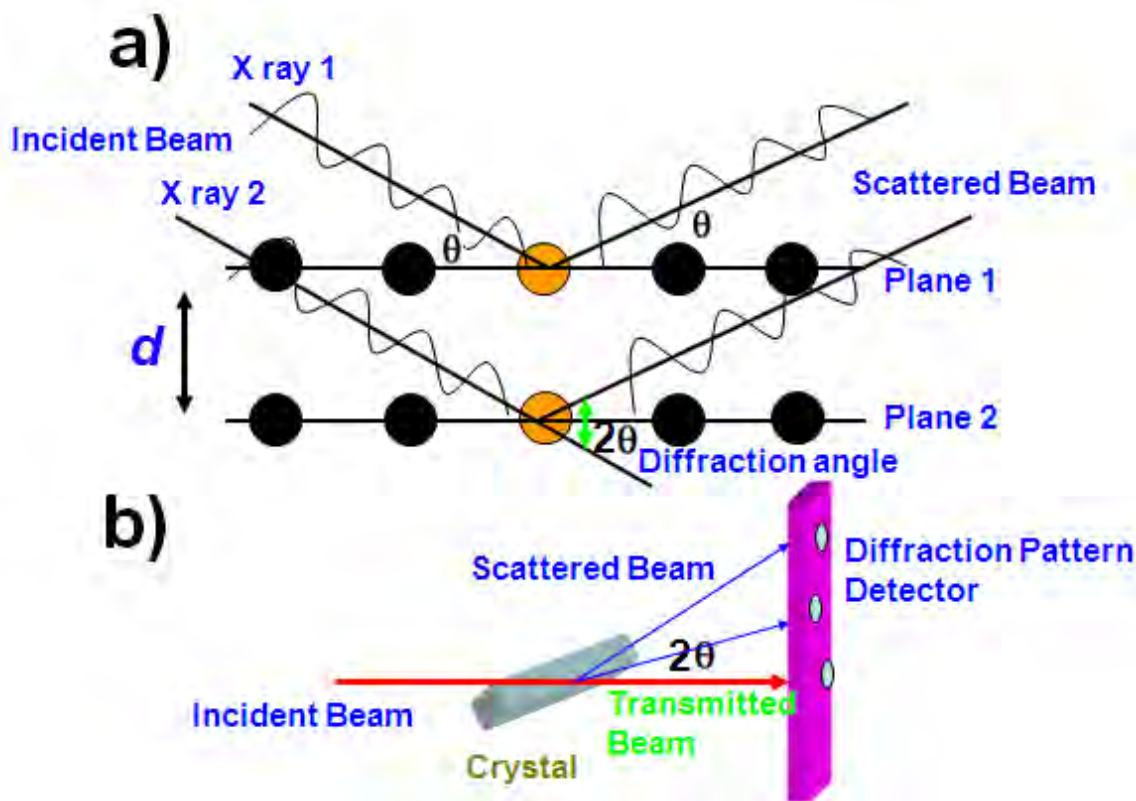


Figure 2.2: Schematic representation for an X-ray Diffractometer.

The theory explained above is valid for crystals in bulk, however, if the samples used are powders (as in our case), there are a huge number of nanocrystals oriented randomly and only the nanocrystals which are oriented in such a way that the Bragg' condition is satisfied, will produce a diffracted beam, then, the theory mentioned before would apply again. In this dissertation, the crystalline phase of the nanophosphors was determined by X-ray diffraction (XRD) using a SIEMENS D-5005 diffractometer with a Cu tube with X-ray radiation at 1.5405\AA , scanning in the $25\text{--}80^\circ$ (2θ range) with increments of 0.02° and a swept time of 2s.

2.2.2 Raman spectra

The Raman effect gives us the vibrational information of molecules when the electromagnetic radiation interacts with them. The Raman scattering is proportional to λ^{-4} , thus, if an infrared laser is used as a source, there is a decrease in the Raman intensity, when compared to that one corresponding to visible lasers. If one photon is absorbed by the molecule and a second one is generated with the same energy, the process is called elastic scattering, then, the molecule did not change after this event. In the case of an inelastic scattering, that is, the Raman effect, the second photon generated is not identical to the first one absorbed by the molecule, the photon can gain or lose energy. If the created photon has less energy than the incident one, this process is called Stokes Raman scattering, if the second generated photon has energy higher than that of the incident one the anti-stokes spectrum is produced. Both processes are reflected in figure 2.3, where ν_0 is the laser excitation frequency and the molecular vibration is represented by ν_v .

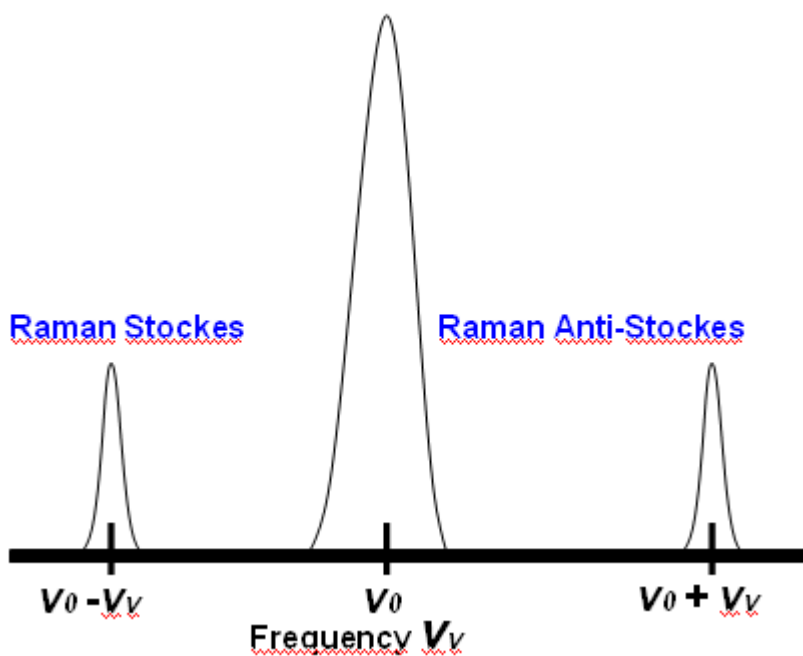


Figure 2.3 Raman and Rayleigh scattering of excitation at a frequency ν_0 . A molecular vibration in the sample is of frequency ν_v .

In this thesis, the Raman measurements in the range of 400-1200 cm^{-1} were taken using an optical microscope which had incorporated the Raman set up to filter the light of the excitation source (laser of 632.8 nm). The parameters for all measurements were: 0.01 mW for optical power and a spot size of the laser around 189 micrometers. In addition, an objective lens of 20X and a total time integration of 30 seg were used. All samples were powders.

2.3 Optical characterization

2.3.1 Absorption measurements

The optical absorption spectra of powders were measured using a Perkin-Elmer UV-VIS-NIR Lambda 900 spectrophotometer which has a 1.5 in. integrating sphere (Labsphere Co) covered internally with the highly reflecting material spectralon. The absorption spectra were taken in the range of 200- 1000 nm. The software included in the spectrometer was used to convert values of diffuse reflectance to absorbance.

2.3.2 Fluorescence measurements

The emission spectra presented in chapters 3 and 4 were obtained using an Acton Pro 500i monochromator and a R955 Hamamatsu photomultiplier tube as detector. The excitation source was a xenon lamp with a total power of 75 watts. The emission spectra were recorded exciting with wavelengths from 290 to 400 nm. The system was controlled with a P C where the emission spectra was displayed and recorded. All photoluminescence measurements were done at room temperature. The alignment of the set up was carefully maintained in order to compare the intensity among emission spectra of different samples.

2.3.3 Infra-Red Fourier Spectroscopy

When molecules are exposed to infrared radiation, they absorb selectively certain wavelengths. The absorption peaks are related to specific vibrational freedom of the molecule and the intensity of absorption peaks is related to the amount of material present. Thus, if the infrared spectrum is analyzed, it is possible to obtain structural information of molecules. FTIR spectrometers (Fourier transform infrared spectrometers) represent the third generation of infrared spectrometers. Those ones have the following advantages over the previous ones such as: faster scanning, and measuring all the infrared frequencies simultaneously, rather than individually. Figure 2.4 shows a scheme for a FTIR spectrometer. It has incorporated a Michelson interferometer, the incident beam coming from a laser is divided using a beamsplitter, one beam is reflected toward a flat mirror which is in a fixed position and the second one is reflected to a mirror which can be moved with variations of milimeters respect to the beamsplitter. The two beams are reflected again from the corresponding mirrors and they are recombined in the beamsplitter, this recombined beam is directed to the detector where the difference in intensity of the two beams is calculated as a function of the difference in the optical path. The resulted signal is an interferogram, which has information about every infrared frequency coming from the source, see figure 2.4, this interferogram is a function of time, to convert it to the frequency domain, the fourier transform is employed. When the sample is put between the beamsplitter and the detector, some infrared frequencies are absorbed and other ones are transmitted, in consequence, the interferogram reflects variations in intensity, those variations have information of the molecular vibrations absorbed from the IR source implicitly, when the fourier transform is applied to this interferogram the frequencies absorbed by the sample (molecular vibrations) are determined.

The infrared Fourier transform (FTIR) measurements were very important to detect impurities in the oxides fabricated in this thesis. It was also useful to find

specific bondings of atoms distributed into the crystalline matrix. Those measurements were recorded in the range of $400\text{--}4000\text{ cm}^{-1}$ on an ABA (MB300) spectrometer using the KBr pellet method [6].

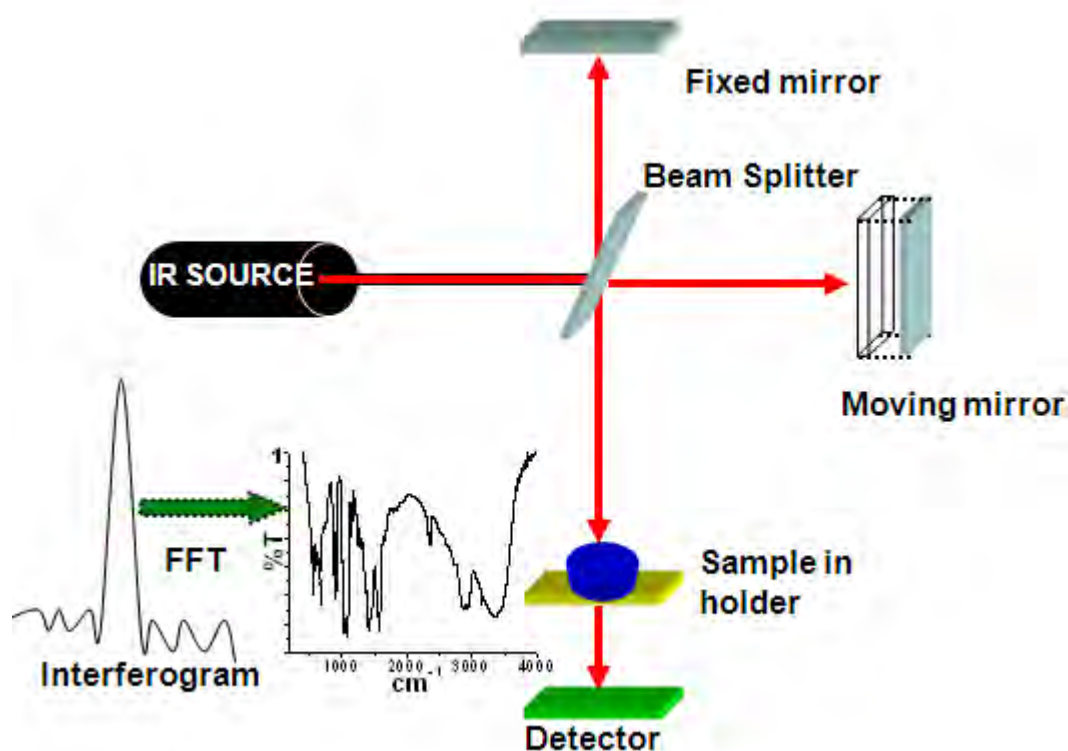


Figure 2.4 Basic setup for FTIR spectrometer.

2.4 Characterization of the Hybrid LEDs

The characterization of the hybrid LEDs fabricated during this work of thesis consisted in obtaining the curves of voltage vs. current (I-V curves) and the electroluminescence curves. The former give us information about the mechanism of injection and transport of electrons through our devices and the second one provides information about the colors emitted by electroluminescence, it also permits us to calculate the CIE coordinates, which are important to know the color's purity. A Keithley 2400 source meter, a fluorometer (see section 2.3.2) and a Photo Research PR-650 SpectraScan

color-photometer were employed to get the I-V curves, luminance and the CIE chromaticity coordinates.

References for chapter 2

[1] B. Fultz, J. Howe, Transmission Electron Microscopy and diffractometry of materials, Springer (2007).

[2] Ludwing Reimer, Scanning Electron Microscopy, Springer Series in Optical Sciences, 1985.

[3] Richard T. Weidner and Robert L. Sells, Elementary Modern Physics, Allyn and Bacon, Third edition, 1980.

[4] Neil W. Ashcroft and N. David Mermin, Solid State Physics, Holt Rinehart and Winston, 1976.

[5] G. Turrel and J. Corset, Raman microscopy: developments and applications. Elsevier 1996.

[6] <http://www.shimadzu.com/an/ftir/support/ftirtalk/talk8/intro.html>

Chapter 3

White light generation from ZnO nanoparticles by photoluminescence and electroluminescence

3.0 Introduction

In this chapter, the optical studies of ZnO quantum dots synthesized with a modified wet chemical method are presented. TEA and dodecylamine (DCA) were used as surfactants, which permitted to tailor the type of defects to produce blue, yellow or white light. When TEA is used, strong blue emission with a quantum yield of 81% was obtained when nanoparticles are dispersed in hexane. Also, yellow emission was obtained by increasing the temperature of synthesis from 60°C to 70°C and using TEA as surfactant. On the other hand, DCA permitted us to control the ratio between yellow and blue bands in the white light emission from ZnO nanoparticles, those nanophosphors had CIE coordinates of (0.32,0.33) which are near of the ideal white light with CIE coordinates of (0.33,0.33). Hence, our results indicate that ZnO quantum dots would be useful to fabricate devices for solid-state applications such as LEDs.

3.1 Synthesis of ZnO nanoparticles and characterization

3.1.1 Synthesis of ZnO

The ZnO nanoparticles were synthesized from an alcohol based solution. All reagents and surfactants with purity higher than 98% were acquired from Sigma Aldrich and used without additional treatments. A solution with 20 gr. of Zinc acetate ($\text{Zn}(\text{O}_2\text{CCH}_3)_2(\text{H}_2\text{O})_2$, ZnAc) and 50 ml of methanol were prepared and then mixed with water in such a way that a ZnAc/H₂O molar ratio of 0.025 was

reached, then dodecylamine ($\text{CH}_3(\text{CH}_2)_{11}\text{NH}_2$, DCA) was added. The mixture was stirred at 60°C for 1h and later 15 ml of hexane was added to induce precipitation. Afterwards, the white powder was separated by centrifugation, washed several times with methanol and dried at 100°C during 1h. Five samples were prepared with different amounts of TEA, 0, 0.5, 0.7, 1.1 and 1.8 ml and tagged as T0, T1, T2, T3 and T4 respectively, see table 3.1.

Table 3.1:

Sample	TEA (ml.)	UV absorption Peak (nm)	Average Size (nm) $\pm 0.4\text{nm}$	Energy Band Gap (eV)	Effective mass Approx. (eV)	Shape	T($^\circ\text{C}$)
T0	0	269	3.5	4.15	4.08	Spheres	60
T1	0.5	273	4.3	4.03	3.81	Spheres	60
T2	0.7	271	4.1	4.06	3.86	Spheres	60
T3	1.1	274	4.5(spheres),5.5 (oval-like)	3.98	3.76	Spheres and oval- like	60
T4	1.8	279	6.3 (spheres), 7.5 nm (oval- like)	3.82	3.55	Spheres and oval- like	60

Two additional samples were prepared with similar conditions but using zinc nitrate and hydroxylamine as surfactant, such samples are identified as T5, and T6. Finally, samples T7 and T8 were prepared by using identical conditions of synthesis than for T3 but in T7, oleic acid was employed as capping agent, while in T8, sodium hydroxide was used as precipitant agent instead of hexane, see table 3.2. Again, other set of samples named T45, T46, T47, T48 were prepared

under the same procedure of T3 to study the yellow and white light emissions. Sample T45 was fabricated at a temperature of 70 °C, and the samples T46-T48 were prepared by using different amounts of dodecylamine ($\text{CH}_3(\text{CH}_2)_{11}\text{NH}_2$, DCA) instead of TEA, see table 3.3.

Table 3.2:

Sample	Zn Precursor (ml.)	Surfactant (ml)	Precipitant	T(°C)
T5	Zinc Nitrate	TEA (1.1ml)	Hexane	60
T6	Zinc Acetate	Hydroxylamine (1.1 ml)	Hexane	60
T7	Zinc Acetate	Oleic Acid (1.1 ml.)	Hexane	60
T8	Zinc Acetate	TEA (1.1 ml.)	NaOH	60

Table 3.3:

Sa mpl e	TEA (ml.)	DCA (ml)	UV absorption Peak (nm)	Average Size (nm)	Energy Band Gap (eV)	Effective mass Approx. (eV)	Shape	T(°C)
T45	1.1	-	254 and 280	5.7	3.58	3.58	spheres	70
T46	-	0.17	281	-	3.61	-	nanoro ds	60
T47	-	0.35	281 and 363	160	3.47	-	nanoro ds	60
T48	-	0.45	281 and 363	-	3.47	-	nanoro ds	60

3.1.2 Structural, morphological and optical characterization

Morphology and crystalline studies of the samples were performed in a High Resolution Transmission Electron Microscopy (HRTEM), FEI- Titan 80-300 KeV. The microscope is equipped with Ultra stable Schottky field emitter gun. The samples were grounded, suspended in isopropanol at room temperature, and dispersed with ultrasonic agitation; then, an aliquot of the solution was dropped on a 3mm diameter lacey carbon copper grid.

Photoluminescence spectra were obtained under 350 nm excitation from a Xenon Lamp (Acton Research Corporation) of 75 Watts. The fluorescence emission was analyzed with an Acton Pro 3500i monochromator and a R 955 Hamamatsu photomultiplier tube for visible emission. All samples were dispersed in hexane for PL measurements. The absorption spectra ranging from 200-800 nm were obtained with a Perkin Elmer lambda 900 spectrometer using a quartz cell of 1 cm of thickness. The IR spectra [Fourier transform infrared (FTIR)] of samples were recorded in the range of 400–4000 cm^{-1} on an ABA (MB300) spectrometer using the KBr pellet method. The quantum yield (QY) of ZnO quantum dots emitting blue light was calculated by using the slope of the curve of photoluminescence versus absorbance of the dye reference quinine sulfate (QS) dissolved in a aqueous solution 0.5M of sulfuric acid (H_2SO_4), see section 3.2 to see details of this calculation. All optical measurements were done at room temperature.

3.1.3 Effect of TEA on the Structure and Morphology of ZnO quantum dots

The crystalline structure of ZnO quantum dots was verified with the Raman spectra of the samples T0, T1 and T3, see Figure 3.1, this graphic shows the $A_1(\text{LO})$ and $E_1(\text{LO})$ modes located in the 540-680 cm^{-1} range as well as other multiphononic lines such as 747 cm^{-1} , 866 cm^{-1} , 938 cm^{-1} , 1027 cm^{-1} and 1078 cm^{-1} corresponding to ZnO wurtzite structure [1,2].

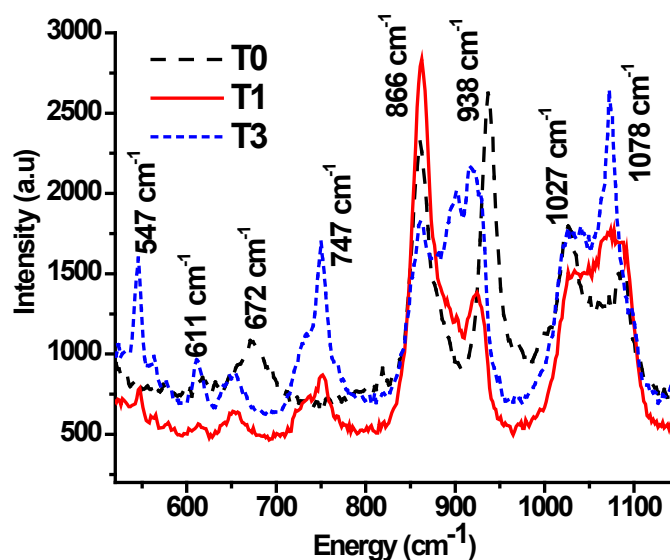


Figure 3.1 Raman spectra of samples T0, T1 and T3.

By comparing the Raman Spectra of the samples T1 and T3 with T0, it was observed that the band centered at 747 cm^{-1} only appeared for samples T1 and T3, suggesting that other ZnO bondings are favored with the presence of TEA. HRTEM images in Figure 3.2a,b show that ZnO nanoparticles are spheres for volumes of TEA below 0.7 ml. (samples T0, T1 and T2), while oval-like nanoparticles mixed with spherical nanoparticles appeared for volumes above 1.1 ml. of TEA (samples T3 and T4), see Figure 3.2c,d.

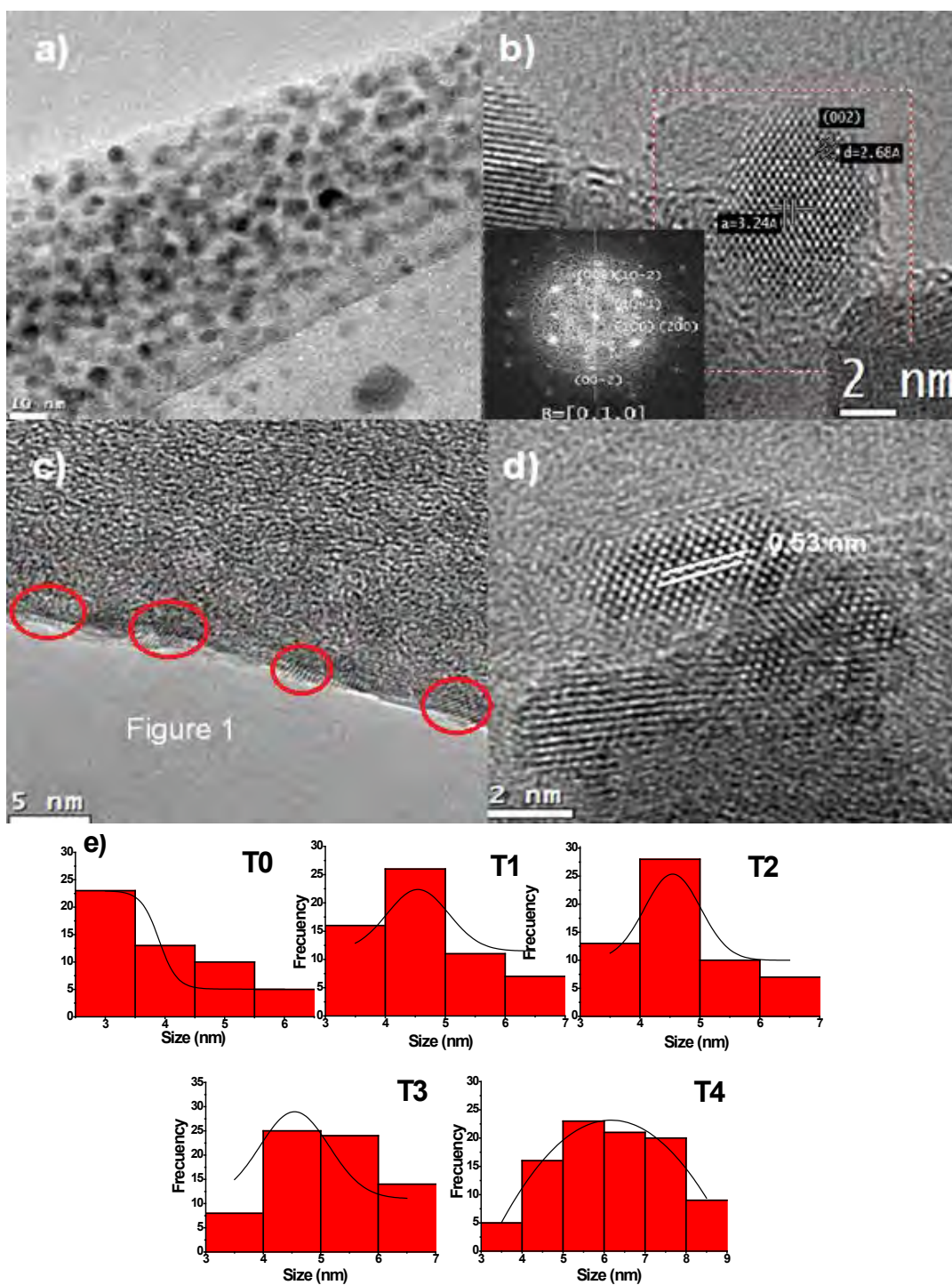


Figure 3.2: HRTEM images of ZnO quantum dots: a) and b) corresponds to sample T2 (0.7 ml of TEA), c) and d) corresponds to sample T3 (1.1 ml. of TEA), e) shows the size distribution of nanoparticles for each volume of TEA. Inset in panel b shows the FFT of spherical nanoparticles with its corresponding crystalline planes.

The ZnO nanoparticles correspond to the spatial group $P6_3mc$ (186) with cell parameters $a=3.2494 \text{ \AA}$ and $c = 5.2038 \text{ \AA}$. In addition, the FFT in figure 3.2b shows the (00-2), (002), (10-2), (10-1), (100), (200,) planes corresponding to hexagonal structure, according to the 36-1451 JCPDS card (obtained from the joint commission for powder diffraction standards). By comparing figures 3.2b and 3.2d, we observed that the distance between crystalline planes increased from 0.324 nm to 0.53 nm, it could be due to the enlargement from spherical nanoparticles to oval-like nanoparticles as consequence of increasing TEA. Spheres in Figure 3.2b corresponding to sample T2 have an average diameter of $4.1 \pm 0.4 \text{ nm}$, and oval-like nanoparticles in Figure 3.2d presented an average length (major axis) and diameter of $5.5 \pm 0.4 \text{ nm}$ and $1.8 \pm 0.2 \text{ nm}$ respectively. Table 1 shows the values of average size of spheres, oval-like nanoparticles and Figure 3.2e presents the size distribution corresponding to each volume of TEA respectively. In general, we observe that the size of nanocrystals increases from 3.5 nm to 6.5 nm as the amount of TEA increases according to the size distribution in Figure 3.2e. In addition, the change from spheres to oval-like could be explained by taking into account that TEA is a capping agent very effective to inhibit the growth of nanoparticles along the c-axis [3]. Also the steric effect, that is, repulsive forces among molecules of the same type, occur predominantly in TEA and thus, it is expected to increase as the amount of TEA increases, therefore after certain amount of TEA (1.1 ml.), only a lateral growth of quantum dots along the a-axis or prism plane [3], is achieved to stabilize nanoparticles, giving raise to oval-like morphology. By continuing with the increase of the amount of TEA (sample T4), the average length of oval-like increased from 5.5 nm to 7.5 nm, the overall length increased because after a volume of 1.1 ml. of TEA, the surface of nanoparticles is saturated, impeding a growth in all directions of individual nanoparticles, then, the Ostwald ripening could occur to form larger nanoparticles with the shape of ovals [4]. Other authors like M.A. Bakar et al. and M. Mamat have reported oval-like nanoparticles above 10 nm by using hexamethylenetetramine as surfactant [5,6].

3.1.4 Effect of TEA on the Absorption and Band Gap of ZnO quantum dots

The optical band gap was calculated for samples T0-T4 and T45-T48 from their absorption spectra. First, the absorption coefficient was calculated by using $\alpha(\nu) \approx (2.303 \times 10^3 A(\nu) \rho) / kL$, where $A(\nu)$ is the absorbance of the sample as a function of frequency ν , ρ is the density of the bulk ZnO, k is the concentration of nanoparticles and L is the thickness of the sample [7], in our case we used the thickness of a quartz cell. Afterwards, this absorption coefficient is introduced in the equation: $(\alpha h\nu)^2 = C(h\nu - EG)$, where C is a constant, $h\nu$ is the energy and EG is the energy band gap, then, to obtain the value of the energy band gap, $(\alpha h\nu)^2$ is plotted versus $h\nu$ and the intersection of the extrapolated linear part of this curve with the axis of energy $h\nu$ give us the value of EG [8], see Figure 3.3a,b to observe the absorption bands and the linear approximation for samples T0-T2.

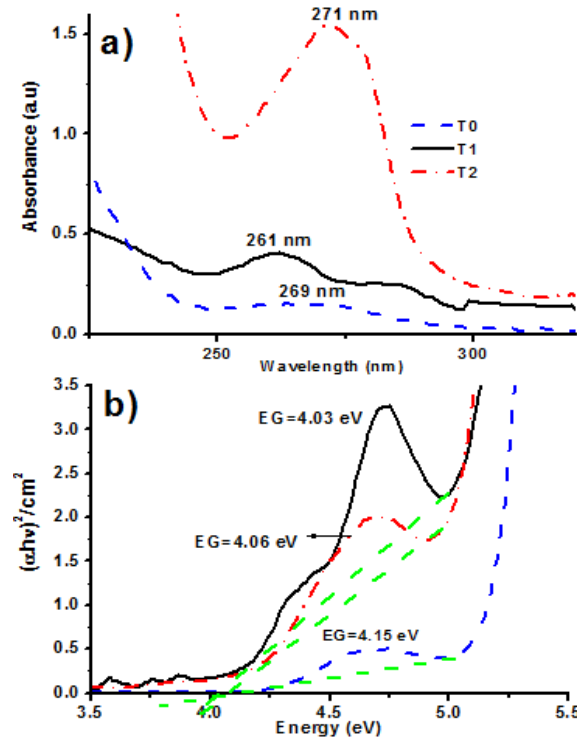


Figure 3.3: a) UV absorption bands and b) $(\alpha h\nu)^2$ vs. $h\nu$, for the samples T0, T1 and T2

In addition, the energy band gap was calculated using the equation of effective mass approximation: $E_g = E_{g,bulk} + \frac{h^2}{8R^2} \left(\frac{1}{m_e^*} + \frac{1}{m_h^*} \right) - 0.248E_{Ryd}$, where E_g is the energy band gap of ZnO quantum dots, $E_{g,bulk}$ is the band gap of ZnO in bulk (3.37 eV), m_e^* and m_h^* are the effective mass of electron and holes respectively, R is the radius of the nanoparticle, h is the Planck's constant and E_{Ryd} is the bulk exciton binding energy (60 meV) [8]. According to results for energy gap in table 1, values of band gap obtained with both methods were similar; the highest difference between those values was 7% taking as reference the values of band gap associated with the linear equation of the absorption coefficient, indicating that our calculations are consistent and with good accuracy. Also from table 1, it is observed that the absorption bands of samples T0-T4 shift to higher wavelengths (without including T2) as the amount of TEA increases, at the same time, the size of the nanoparticles increases and the energy gap values decrease. Then, as the amount of TEA increases the quantum confinement effect raises because the size of nanoparticles is near of the bulk exciton Bohr radius $a_B=2.34$ nm, that is, the enlargement of energy band gap by decreasing size of nanoparticles, will be approaching to the value of 3.37 eV for the bulk in ZnO. This increase in the BG as the sizes of nanoparticles decreases is in agreement with other works reported in the literature [9]. However, the sample T2 is not in agreement with the trend of quantum confinement, this difference could be caused by the "sharpeness" of the absorption peak for this sample (the absorption measurements for this sample were reproduced 3 times), the absorption bands of the other samples are broad, see Figure 3.3a, but the absorption of T2 is not so broad like the other samples, thus the slope of the curve of $(\alpha h\nu)^2$ versus $h\nu$ for this sample T2 will be out of the general trend. The decrease of the width of sample T2 compared to samples T0 and T1 could be caused by a decrease in the absorption of the types of defects presented in the sample T2. In the case of samples T3 and T4 which contained spherical and oval-like nanoparticles, an increase in TEA produces lower EG values. This diminution could be explained considering that a higher volume of TEA increases

the average length of oval-like nanoparticles, from 5,5 nm (sample T3) to 7.5 nm (sample T4), that in turn shifts the absorption band to longer wavelengths, therefore decreasing the value of EG. It is worth to notice that the obtained EG values for spheres and oval-like are higher than these reported by other authors [7-9]. This could be explained taking into account that the sizes of the spheres, see table 1, are near the value of 2.34 nm corresponding to the exciton Bohr radius of ZnO bulk, thus ZnO quantum dots with morphology of spheres present strong confinement effects. In addition, ZnO oval-like nanoparticles also present strong confinement because their radius is less than 2 nm [10], therefore EG values are enhanced. N.R. Yogamalar et al. have reported energy band gap values around 4 eV with sizes ranging from 17 to 25 nm, this suggests that our results are reliable because we have lower nanoparticles sizes [7].

3.1.5 The Role of TEA on Impurities

A comparison of FTIR spectra for T0 and T1-T4 synthesized with and without TEA, see Figure 3.4, evince the presence of TEA on the ZnO surface. The bands centered at 2926 cm^{-1} , 1065 cm^{-1} , 893 cm^{-1} and 613 cm^{-1} associated to TEA do not appear in the sample T0 [11]. Meanwhile, the bands related with the residual acetate (COOH groups) centered at 1409 cm^{-1} and 1569 cm^{-1} appears in all samples [12]. In addition, the band centered at 3352 cm^{-1} associated to OH groups as well as the bands associated to COOHs decrease as TEA increases, reaching a maximum for the volume of 0.5 ml. and then decreases for higher volumes. The bands associated to COOH groups are important because those protect the surface of ZnO quantum dots against the adherence of OH groups which could be detrimental for emission and stabilization of such nanoparticles in hexane or methanol [13]. The degree of capping on nanoparticles is determined by the amount of acetate groups and TEA which remain in the surface of the quantum dots. Capping helps to stabilize the quantum dots in hexane as well as to increase the emission of nanoparticles by removing OH groups, as discussed

in the next sub-section. Samples T4 and T0 are similar even though the conditions of synthesis are different, this will be explained in section 3.2.2.

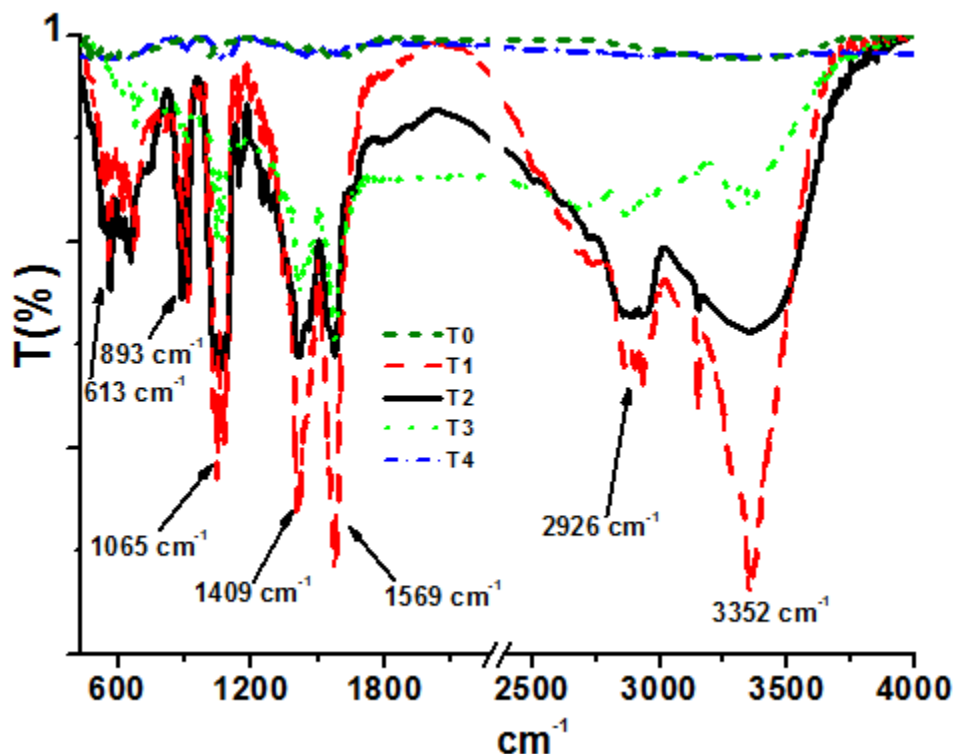


Figure 3.4: FTIR spectra of sample T0 prepared without TEA, and samples T1-T4 prepared with different volumes of TEA.

3.2 Photoluminescence measurements

3.2.1 Blue Emission and Origin of Defects Produced by TEA

The photoluminescence (PL) and photoluminescence excitation (PLE) spectra of the samples T0 (synthesized without TEA) and T3 (synthesized with TEA) which presented the best blue emission in hexane are shown in Figure 3.5a. Both samples presented a blue emission band centered at 429 nm (2.89 eV) under 350 nm excitation, but the overall emission of sample T0 was 7.5 times lower.

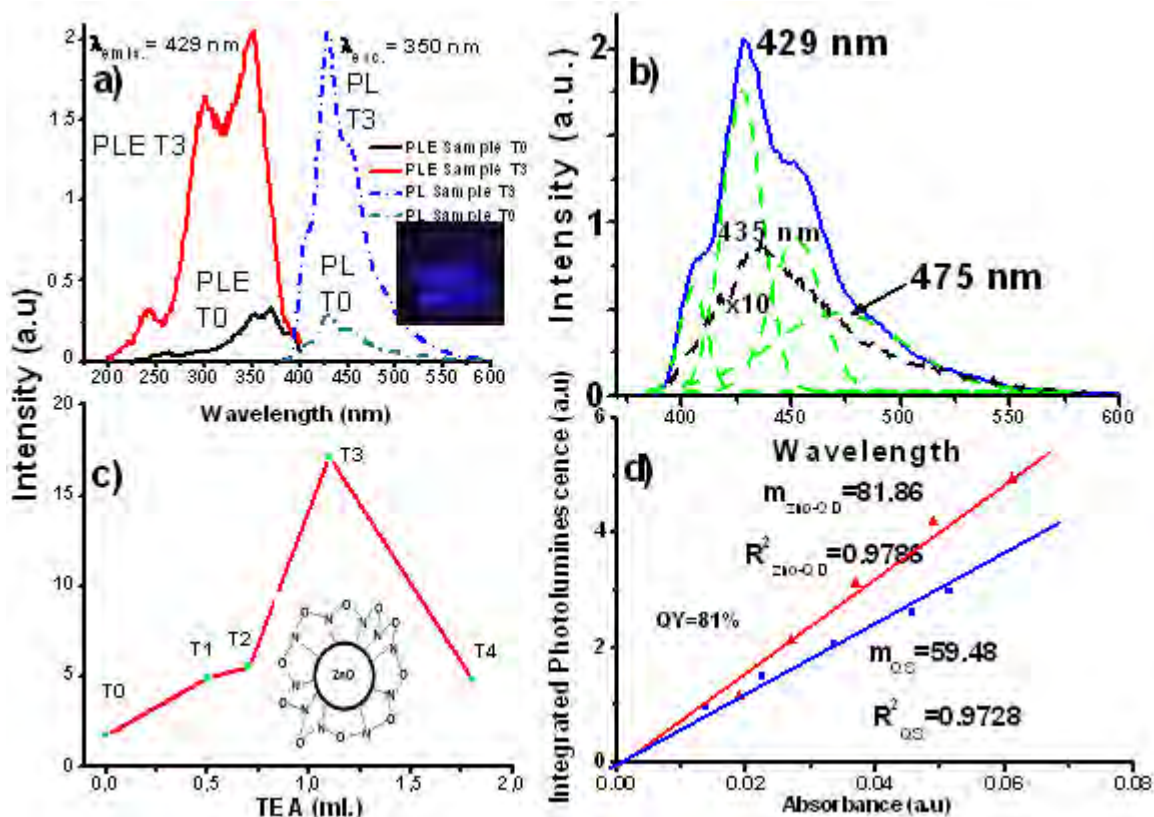


Figure 3.5: a) PL and PLE spectra of sample T0 (without TEA) and T3 (with TEA), b) PL spectra of sample T3 dispersed in hexane (blue curve) and methanol with Gaussian fitting (green curves), c) Integrated photoluminescence as function of TEA volume and d) Fitting used to calculate the quantum yield (QY) of ZnO quantum dots dispersed in hexane.

Furthermore, it is observed that the PLE for sample T3 has an extra band centered at 300 nm in comparison with the excitation spectra of the sample T0. Thus, higher emission with introduction of TEA and additional excitation wavelengths, suggest that TEA increases the amount of surface states by surface-bonded TEA on the ZnO quantum dots, see Figure 3.5c. This effect of increasing defects is the opposite of that reported by M.L. Singla et al., they observed that the presence of surfactants (CTAB, TOAB and PVP) on the surface of ZnO nanocrystals decreases the amount of defects that produce visible emission [14]. The attachment between the molecule of TEA and the

surface of ZnO could be caused by OH groups and amines coming from TEA, therefore the amine can remain on the surface of ZnO also, which interacts with the Zinc or Oxygen atoms in the surface of nanocrystals, that in turn could produce Zn interstitials or Zinc vacancies which originate blue emission according to literature [15,16]. In fact, we expect to have Zn interstitial defects since they are formed in Zn rich vapor environments [16], and our synthesis procedure involved vapor coming from methanol boiling at 60°C as well as Zinc acetate as precursor. This assumption could be corroborated from the Raman spectra, since the samples with TEA showed more Raman peaks related with the crystallinity of ZnO, see Figure 3.1, this means that atomic rearrangements of the crystalline lattice are carried out and consequently, Zinc interstitial defects related with blue emission could appear. According to Fu et al. Carboxylate complexes formed by the reaction of hydroxyl and carboxyl groups could be responsible for the blue emission [9]. In our case we have hydroxyl groups coming from TEA and COOH groups coming from ZnAc, then it can be assumed that our emission should be associated to carboxylate groups again; however, we prepared one sample with Zinc nitrate instead of ZnAc and we recuperated a strong blue emission. This result points out that the blue emission could be produced by interaction between amines and the surface of ZnO as explained above and carboxylate groups are not essential to produce blue emission. In order to understand how Zinc interstitial defects are formed during synthesis, a solution of TEA and methanol was prepared under the same conditions of synthesis than for ZnO quantum dots, after irradiation with 350 nm no emission was observed. From this point, it is supposed that the emission comes from ZnO nanoparticles. Some authors have reported that the formation and emission of defects in ZnO is caused by the presence of a surfactant or the surface-bonded organic molecules on the surface of nanoparticles, that in turn, are responsible for the creation of surface states that generate visible emission [8,14]. In our case, surfactant is not indispensable to create defects that originate blue emission because it was observed without the presence of surfactant (TEA), see emission spectra of sample T0 in Figure 3.5a. However, TEA helps in the formation of Zn Interstitial

defects since it increases the luminescence of nanoparticles as explained before. To understand the role of TEA on the creation of such defects, additional samples T5-T8 were synthesized, see table 2.

First, it should be demonstrated that the formation of carboxylate groups as result of the reaction between hydroxyl groups coming from TEA and carboxyl groups coming from zinc acetate, is not vital for the formation of defects that produce blue emission as affirmed by other authors [8]. For this, sample T5 with Zinc nitrate using the same conditions of synthesis that for T3 was synthesized, in this way the carboxyl groups (COOH) are not introduced. After photoluminescence characterization, see Figure 3.6, the same blue band appears with an integrated intensity of 93% in comparison to sample T3. This indicates that the formation of carboxylate groups is not the origin of defects for blue emission.

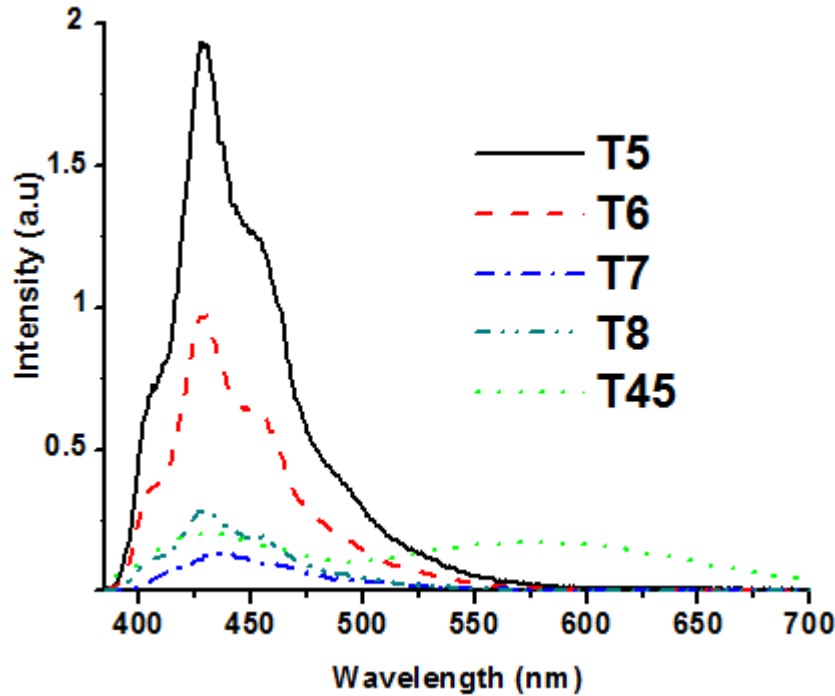


Figure 3.6: PL Spectra of samples T5, T6, T7, T8 and T45 excited under 350 nm.

Second, the photoluminescence characterization of the sample T0 synthesized without TEA, showed the same blue band than the samples T1-T4. Thus, the

creation of defects responsible for the blue emission could be due to the thermal treatment as well as the method of precipitation during synthesis. Also, this result suggests that the presence of a surfactant is not necessary to have defects after fabrication. TEA contains an ammine which is necessary for the formation of defects, since a difference of 7.5 times in emission intensity was obtained between the samples T3 and T0. If the ammine group is responsible for the blue emission, then blue light should be observed by using another surfactant that contains an ammine. To confirm this assumption, sample T6 was fabricated using the same procedure that for T3 but hydroxylamine was used as surfactant. Photoluminescence measurements for sample T6 showed the same blue band but the overall emission was at about 50% lower than for the sample T3, see Figure 3.6. This diminution in intensity could be associated with the amount of OHs introduced by the hydroxylamine, since this molecule only has one OH chain attached to the Nitrogen atom, therefore the probability of an ammine (which creates defects for blue emission) to be attached on a nanoparticle should be less than for TEA which contains three chains of OH groups. The following step was the fabrication of another sample under the same conditions of synthesis used for T3 but the surfactant was oleic acid which does not contain an ammine (sample T7). After PL measurements in hexane, a weak blue emission with an integrated emission of 10% taking as reference the sample T3, was observed at 435 nm, see Figure 3.6. This shifting in the blue band to longer wavelengths when oleic acid is used indicates that other types of defects are formed when surfactants which do not contain an ammine are used. This corroborates the role of ammine to produce mainly defects emitting at 429 nm. Hence, ammine enhances the amount of surface states on nanoparticles that in turn produce blue emission. Furthermore, the hexane precipitant has an important role to form defects: Sample T8 was fabricated with the same conditions of synthesis that for sample T3 but sodium hydroxide (NaOH) was used as precipitant agent, its PL spectra showed a weak blue emission at 429 nm, see Figure 3.6. This supports the idea that the formation of defects depends on the concentration of OHs on the surface of nanocrystals, since it is expected a

decrease in the signal because NaOH introduced OHs which would be detrimental for emission, but hexane does not introduce such OHs, facilitating the conservation of defects which were formed during synthesis. Those results suggest that the formation and conservation of defects is not possible with the only presence of TEA or hexane individually during synthesis. Hence, the combined presence of TEA and hexane produces and preserves more defects than such produced by the solely presence of TEA or hexane.

By decomposing the blue emission spectra of sample T3 in its Gaussian components, see Figure 3.5b, it was found that such spectra is the result of the overlapping of emissions at 429 nm, 435nm and 475 nm. The structure of the blue emission band centered at 429 nm did not change regardless of an increase in the amount of TEA, indicating that other type of defect (oxygen vacancies, zinc vacancies etc.) are not formed when the amount of TEA is increased, if another kind of defects appeared in the samples with TEA, we should observe for example green or yellow emissions, but it did not occur, thus the Zinc interstitial defects that produce emission peaks at 429 nm, 435 nm and 484 nm are stable. The structure of the photoluminescence spectra of the sample T3 was identical than those of samples T1, T2 and T4 (not showed here). Those spectra did not show UV emission at 390 nm (associated to energy gap of ZnO) when excited with 350 nm, this could be due to a “screening effect” produced by the blue emission, that is, the excitation wavelength excites preferably the surface of ZnO nanocrystals which originates blue light instead of the “bulk” of the nanocrystals with better crystallinity which can produce 390 nm emission. The emission at this UV wavelength is typical for high crystalline ZnO [17,18].

3.2.2 Effect of TEA on the Luminescence of ZnO quantum dots

Figure 3.5c shows that the content of TEA increases the integrated blue emission, reaching a maximum for a volume of 1.1 ml. and then decreases. This increase in luminescence with the content of TEA could be explained taking into

account that the amount of impurities such as OHs (3352 cm^{-1} band) that quench luminescence in ZnO quantum dots decreases as the amount of TEA increases, see FTIR spectra in Figure 3.4. To better understand the effect of OH groups on the luminescent properties of nanoparticles dispersed in a hydrophobic medium like hexane, we carried out photoluminescence measurements of ZnO quantum dots dispersed in methanol, as observed on the black dotted curve in Figure 3.5b (zoomed 10 times), the blue emission was 95% lower compared to that of T3, indicating that the presence of OHs decreases the luminescence. This diminution on emission intensity evinces that our nanoparticles are hydrophilic, when they are dispersed in methanol the OH groups in this medium attach to OH groups that are capping the ZnO nanoparticles, reducing the surface states that produce blue emission [19]. Nevertheless if nanoparticles are dispersed in a hydrophobic medium like hexane (C_6H_{14}), they are dispersed due to the steric effect, avoiding attaching of OH (not present in hexane) and conserving the surface states that produce blue light. Hence, OH groups acting as capping around nanoparticles benefit emission when they are dispersed in a hydrophobic medium as hexane and are detrimental for emission when quantum dots are dispersed in a hydrophilic medium such as methanol. The integrated blue emission of the sample T4 is lower than T3, suggesting that after certain volume of TEA more defects can not be formed in such way that emission would increase. If we continue adding TEA after 1.1 ml. of volume, the polymeric capping formed with the OH chains and amines coming from TEA will increase in such way that it would decrease the luminescence of nanoparticles. This polymeric capping could be formed in the following way: 1) From a volume of TEA of 0.5 ml., ammine and OH groups attach on the surface of ZnO forming Zn interstitial defects, 2) if we increase the amount of TEA (volumes of 0.7 and 1.1 ml.), several OHs react to release H_2O and at the same time a complex network, i.e., oxygen bridges between ammines (polymeric capping) are formed, see inset Figure 3.5c, this produces a diminution of the amount of OH groups and by consequence TEA molecules on the surface of ZnO also decreases, see FTIR in Figure 3.4, that in turn, produces an enhancement of the blue emission coming from defects. 3) If

we continue increasing TEA (1.8 ml.), the surface of ZnO nanocrystals is over-saturated and the thickness of capping should increase, then not only ZnO nanoparticles are more difficult to reach under an excitation of 350 nm due to the thickness of capping but also the emission of defects could be quenched by absorption of the blue photons in the polymeric capping. Furthermore, if defects are excited to produce blue (sample T4), the blue photons could be absorbed. It may also explain why the luminescence decreased from T3 to T4. Finally, the sample T4 synthesized with TEA had stronger integrated emission than T0 see Figure 5b. From here, we can assume that the amount of defects produced in T4 should be higher than in T0, since both samples have similar content of impurities according to FTIR in Figure 3.4. This behavior corroborates that TEA used during synthesis augments the amount of defects, which in turn raises luminescence.

3.2.3 Quantum Yield

The quantum yield (QY) of ZnO quantum dots dispersed in hexane was calculated using quinine sulfate (QS) as a reference. Five concentrations of ZnO quantum dots emitting blue light dissolved in hexane (refractive index of hexane $\eta_{ZnO} = 1.375$) and QS dissolved in sulfuric acid (refractive index of aqueous solution $\eta_{QS} = 1.33$) were made. Afterwards, the integrated photoluminescence and absorbance values of each concentration under 350 nm excitation were obtained. All absorbance values were less than 0.1. Also, the excitation and emission slit width was 100 nm during PL measurements. Later, the QY of ZnO quantum dots was calculated by comparing the integrated photoluminescence intensities and the absorbance values of ZnO nanoparticles (sample T3) with the corresponding values of the reference quinine sulfate. By using the slope values from figure 3.5d and the equation: $QY = QY_{QS} (0.55) (m_{ZnO} / m_{QS}) (\eta_{ZnO}^2 / \eta_{QS}^2)$, where QY_{QS} is the quantum yield of quinine sulfate (0.55), m_{ZnO} and m_{QS} are the slopes from the lines in the curves of the integrated emission intensity versus absorbance, η_{ZnO} and η_{QS} are the refractive index of hexane and quinine sulfate

respectively [8], a value of QY=81% was obtained. This result indicates that TEA is very effective to increase the efficiency of blue emission of ZnO quantum dots, even more than oleic acid which helps to produce blue emission with a quantum yield of 76% [20]. In addition, this value points out that those nanoparticles could be used for biolabeling in which high emission as well as photostability is important to get images with good contrast [21].

3.2.4 Yellow Emission

By increasing the temperature of synthesis of the sample T3 from 60°C to 70°C, evaporation of methanol is carried out faster, therefore agglomeration of nanoparticles is easily achieved, HRTEM images in Figure 3.7 of the sample T45 showed those clusters of nanoparticles with nanocrystals with an average size of 5.7 nm, then an increase in size of 1.2 nm with respect to sample T3 is produced, see tables 1 and 3.

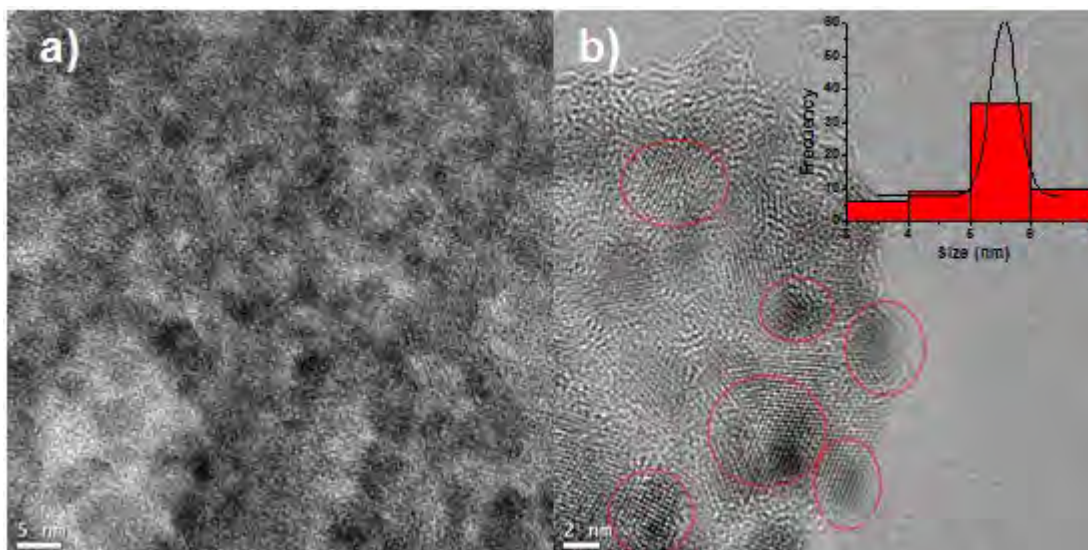


Figure 3.7: HRTEM images of the sample T45 synthesized with TEA at 70°C. Inset shows the size distribution of nanoparticles.

By comparing the size distribution of samples T3 and T45, it is clearly observed that most nanoparticles are now in the range of 5-6 nm instead of 4-5 nm as shown in Figure 3.2e. In general those nanoparticles emitting yellow light are less

dispersed than nanoparticles synthesized with TEA at 60 °C, compare figures 3.2a and 3.7a. Consequently, an increase in size as well as conglomeration of nanoparticles could be related with the change of emission from blue to yellow when temperature is increased to 70 °C during synthesis. Moreover, FTIR spectra in Figure 3.9b indicated that the amount of impurities such as CO₂, TEA and OH groups are lower for the sample T45 in comparison to T3, it is expected lower concentrations of impurities as a result of lower surface area which is caused by an increase in size of nanoparticles. Figure 3.8a shows the emission of those ZnO nanoparticles under 350 nm excitation, a small blue component centered at 438 nm and a predominant yellow component centered at 592 nm are observed.

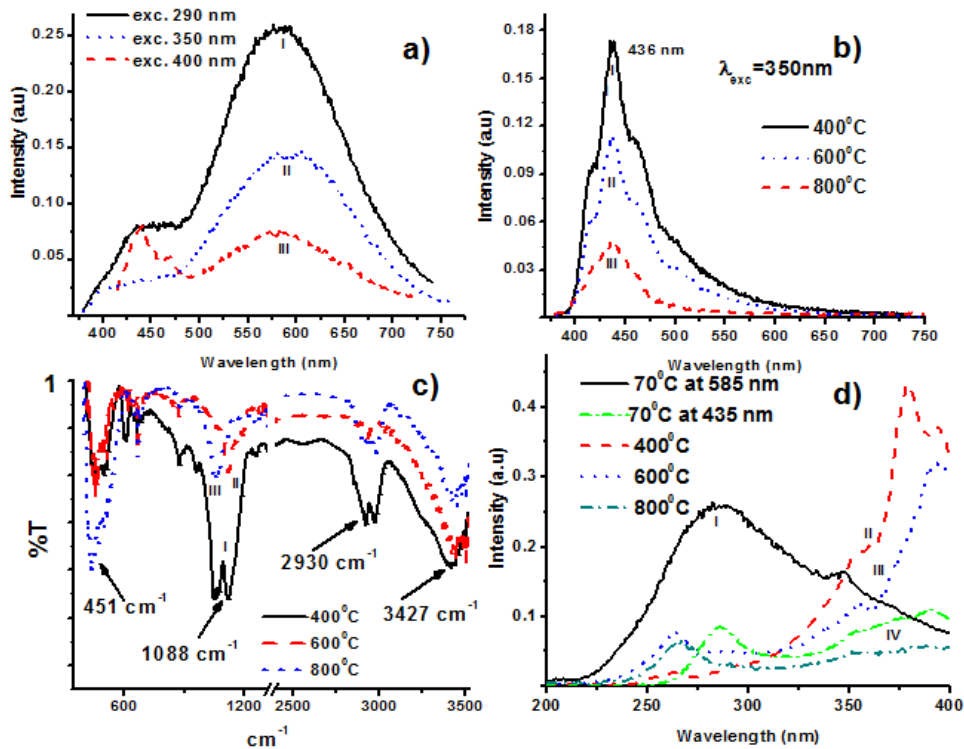


Figure 3.8: a) Emission spectra of T45 excited under: I) 290 nm, II) 350 nm and III) 400 nm, b) and c) are the emission and FTIR spectra of T45 annealed at I) 400°C, II) 600°C and III) 800°C, d) Excitation spectra ($\lambda_{exc}=590$ nm) of T45 annealed at: I) 70°C II) 400°C, III) 600°C and IV) 800°C.

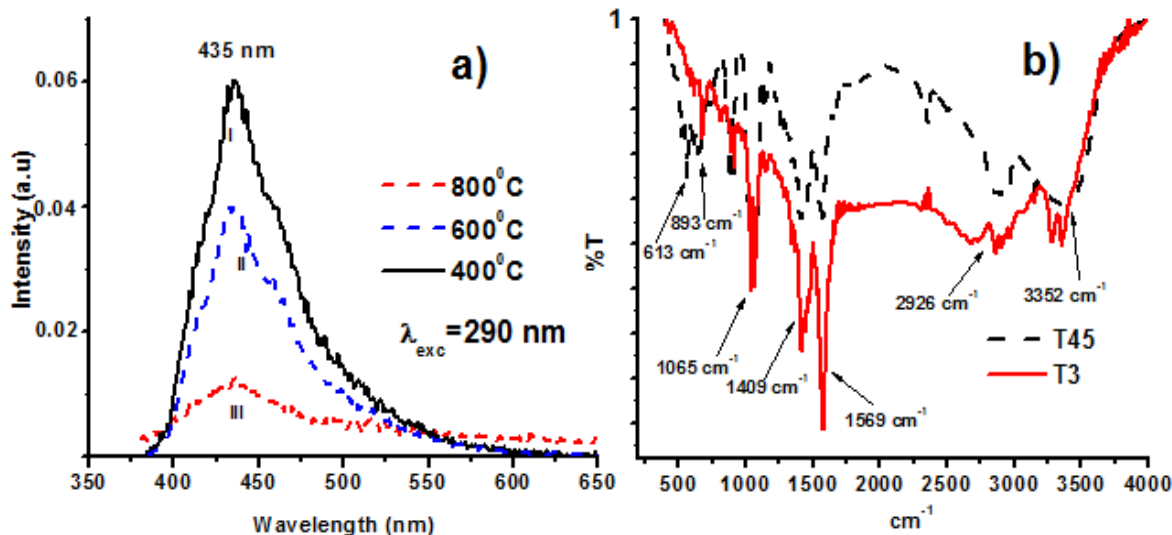


Figure 3.9: a) Emission Spectra of T45 annealed at: I) 400°C, II) 600°C and III) 800°C, under 290 nm excitation, and b) FTIR spectra of T45 and sample T3 synthesized at 70°C and 60°C respectively.

To elucidate the type of defects that produce yellow emission, sample T45 fabricated at 70°C was annealed at 400°C, 600°C and 800°C in a furnace under air atmosphere. It was found from this thermal treatment that those samples presented blue emission under 350 nm excitation. Such emission decreased as the annealing temperature was increased and the yellow emission disappeared completely, suggesting that oxygen vacancies are related with yellow emission [22], see Figure 3.8b. When annealing of ZnO are achieved in air, oxygen atoms are incorporated in the crystalline structure, filling the vacancies. Therefore, the yellow emission disappeared. According to literature, under very reducing conditions and high temperatures, oxygen vacancies could predominate [23]. In our case, the temperature of 70°C is above the boiling point of methanol (65°C) and was reached rapidly from 60°C, this could produce high local temperatures among nanoparticles whereas they are formed as clusters. Consequently, we can assume that oxygen vacancies could be related with the yellow emission. If we increase temperature, organic impurities are removed (TEA residuals, COOH and OH groups) and oxygen coming from air can react with Zn to form ZnO with better crystallinity, this is corroborated with an increase in absorption of the band at 451 cm⁻¹ associated to the free-surface ZnO, and a reduction in the bands at

1088 cm^{-1} , 2930 cm^{-1} and 3427 cm^{-1} associated to COOH, TEA and OHs respectively, see the FTIR spectra in figure 3.8c. Blue emission appears and it decreases as the temperature is raised from 400 $^{\circ}\text{C}$ to 800 $^{\circ}\text{C}$, see Figure 3.8b. Then, the blue emission is reduced because defects disappeared to get better crystalline structure. The amount of defects emitting blue light at 400 $^{\circ}\text{C}$ is lower than those formed with interaction of amines with the surface of ZnO nanoparticles synthesized at 60 $^{\circ}\text{C}$ or 70 $^{\circ}\text{C}$, compare blue emission of figures 3.5a and 3.8b, this means that lower temperatures along with amines favor blue emission. In addition, the blue emission at 400 $^{\circ}\text{C}$ has been also observed by H. Zeng et al., they demonstrated that the blue emission at high temperatures is caused by Zn interstitial produced by non-equilibrium processes (such as laser ablation and zinc-rich annealing) and the decrease of blue signal as annealing temperature increases is due to the outward diffusion of Zn interstitials [24]. Hence, the blue emission that we obtained at high temperatures should be caused by Zn interstitials again, since the structure of blue emission bands is very similar to that of low temperature. Figure 3.8d shows the excitation spectra of the as-prepared sample T45 at 538 nm as well as of the annealed samples at 400 $^{\circ}\text{C}$, 600 $^{\circ}\text{C}$ and 800 $^{\circ}\text{C}$. If we compare the excitation spectra of the sample T45 at 70 $^{\circ}\text{C}$ with the rest of samples, it is observed that the broad band centered at 290 nm disappeared, it is possible to associate this band to defects that produce yellow emission since under excitation at 290 nm, only the sample at 70 $^{\circ}\text{C}$ emitted yellow light, see Figure 3.8a, whereas the rest of annealed samples emitted only weak blue light, see Figure 3.9a. In addition, a difference in the structure of excitation is observed among the sample at 70 $^{\circ}\text{C}$ and the others. The main excitation bands suffered a shifting from 290 nm to the 350-400 nm range, from here, it is possible to conclude that this change in the excitation bands after annealing is related to the change of type of defects in the ZnO nanocrystals, from oxygen vacancies to zinc interstitials. On the other hand, the absorption spectra of the blue-emitting nanoparticles (sample T3) and yellow-emitting nanoparticles (sample T45) have the same absorption bands centered at 263 nm and 280 nm (not shown here). The simultaneous appearance of those two peaks

in the absorption spectra of both samples despite their difference in size (1.2 nm) and emission as well as the fact that the ZnO without surfactant (sample T0) has an absorption band centered at 269 nm, indicate that we can not see the effect of the changes in size or emission reflected in the absorption bands as a consequence of the change in temperature of synthesis, and that the shoulders at 263 nm and 280 nm should correspond to defects. The nanoparticles of sample T45 are even more conglomerated in comparison with those ones corresponding to sample T3, compare figures 3.2a and 3.7a, this conglomeration produced bigger nanoparticles, which contain oxygen vacancies responsible of yellow emission. If the size of the nanoparticle is big enough, the effect of confinement disappears and it cannot be distinguished in the absorption measurements [25]. From here, it is concluded that the defects formed are stable because there is no change in absorption bands in spite of a slight increase in size and shifting in emission from blue to yellow, which occurred when temperature was increased from 60°C to 70°C.

3.3 White Light Emission

We increased the size of ZnO spherical nanocrystallites from 3.5-8 nm to nanorods ranging in size from 125 to 185 nm by using the same method of synthesis at 60°C but TEA was substituted by dodecylamine ($C_{12}H_{27}N$, DCA), see HRTEM images in Figure 3.10.

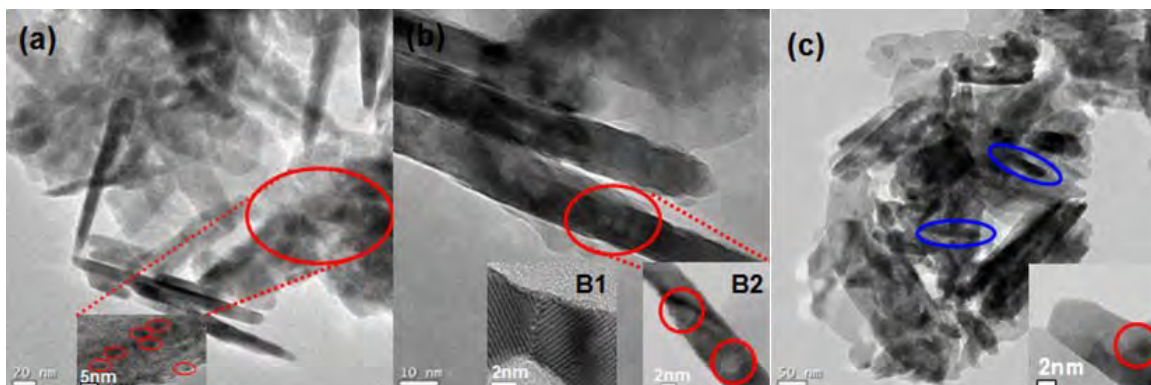


Figure 3.10: HRTEM images of the sample T47 synthesized with dodecylamine.

Most nanoparticles are in the range 145-165 nm and the average size of all nanoparticles was 160 nm. It can be observed in Figure 3.10a,c that nanorods are rounded with a capping agent which would be dodecylamine as indicated by the bands centered at 736 cm^{-1} , 2859 cm^{-1} and 2925 cm^{-1} in Figure 3.11b, and those nanorods are forming conglomerations along with smaller nanoparticles distributed around them, see figure 3.10a,b. Also, some nanorods are assembled together by its lateral side. According to these results, nanorods seems to be formed by assembling from smaller nanoparticles which could be nanorods units as encircled in blue in Figures 3.10c that in turn are formed from quantum dots. Those conglomerations of quantum dots could be observed like clouds encircled in figure 3.10a. Furthermore, this change from QDs to nanorods is reflected in the absorption spectra because a new band appeared at 363 nm, and the band related to defects producing blue emission changed in average from 270 nm to 281 nm, this shifting in absorption could affect the blue emission since it changed from a band centered at 429 nm to a broader and less sharp band centered at 435 nm as discussed below, compare Figures 3.11a and 3.3a.

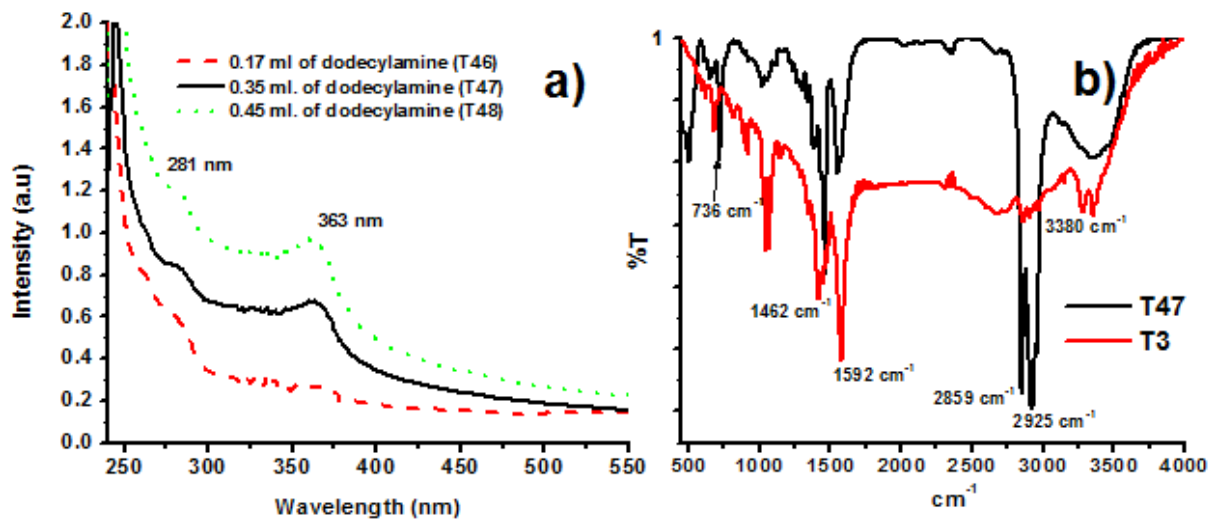


Figure 3.11: a) Absorption spectra of the samples: T46, T47 and T48 and b) FTIR spectra of the sample T47 and sample T3 synthesized at 60°C .

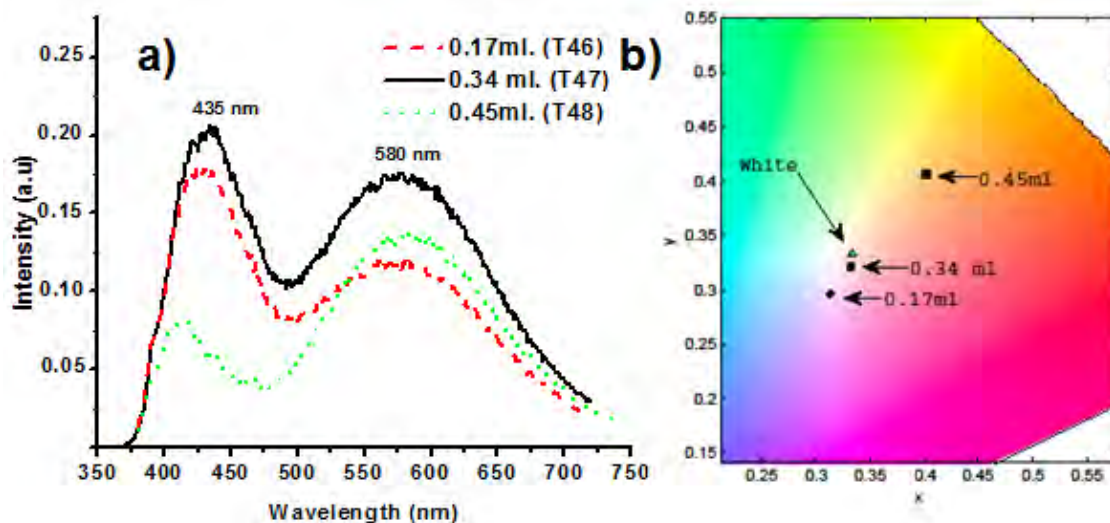


Figure 3.12: a) Photoluminescence Spectra of the samples T46, T47 and T48, b) Diagram for the CIE coordinates for samples T46-T48.

The origin of blue emission could be the same as explained before, that is, from surface defects which are formed due to the interaction of amines coming from DCA and the surface of ZnO (Zinc interstitial defects) while the yellow emission is originated from oxygen vacancies. Both types of defects should be contained in nanorods to produce white light, above all if they were made by assembling from QD containing Zn Interstitials and Oxygen vacancies as explained before, then, such defects should be conserved in nanorods. Other possibility is that the combined emission from nanorods and smaller nanoparticles (nanorods units and clouds formed with QDs) generates white light, but in this case we need to know the contribution of each type of nanoparticle to the emission bands, which is out of the scope of this work. By comparing the blue emission of the sample T47 with those of samples T3 and T6 which contained TEA and Hydroxylamine respectively, see Figures 3.5 and 3.6, it is seen that the blue emission band of T47 is the same that for T3 and T6, then Zn Interstitials located in ZnO quantum dots can be associated to the blue component in the white light emission. Further, the absence of OH groups in the DCA could be a key factor to produce oxygen vacancies along with Zn interstitials because we obtained mainly defects related with yellow emission or blue emission when was employed TEA at a

temperature of 60 °C or 70°C. On the other hand, the diminution of the acetate groups at 1462 cm⁻¹ and 1592 cm⁻¹ in the sample T47 in comparison with T3 and the OH groups at 3380 cm⁻¹ on ZnO nanocrystals, see Figure 3.11b, indicates that by employing DCA the chemical reaction was more effective and energetic than using TEA to liberate COOH groups from ZnO and to consume OH groups coming from methanol to produce hydrolysis. This can be corroborated taking into account that the band related with OH groups in the sample T47 is lower in comparison with the sample T3, see Figure 3.11b. Consequently, Dodecylamine acted as a fuel event though at low temperatures since the agglomeration of nanorods and smaller nanoparticles was obtained, see figure 3.10. The presence DCA is important because its ammine could act like an anchor among nanoparticles that emit blue (with a size of 3-8nm) and yellow light (with a size of 20-50 nm), and therefore promoting the coalescence to form nanorods with both types of defects. It is possible to tailor the ratio between the blue and yellow bands with the amount of DCA introduced during synthesis, see Figure 3.12a. In this way, we can tune the overall emission from cool white light to warm white light, the CIE coordinates were (0.313,0.295), (0.332,0.321) and (0.401,0.406) for the samples which contained 0.17 ml. (cool white), 0.34 ml.(ideal white), and 0.45 ml. (warm white) of dodecylamine respectively, see Figure 3.12b. From here, we deduce that variations in the volume of DCA permit to change the amount of ZnO nanoparticles that produce yellow and blue emissions as explained before, but if we use only TEA, it is not sufficient to produce particles with both types of defects, we can produce nanoparticles emitting predominantly in the blue or in the yellow band. Those results demonstrate that our ZnO nanoparticles fabricated with dodecylamine could be a good choice to fabricate ZnO based LEDs emitting white light.

3.4 Schematic for defects emitting blue and yellow light

The mechanisms of the yellow and blue emission can be understood by exciting with energies above and below the band gap of ZnO nanoparticles. By using the

excitation spectra of samples T0, T3 and T45, see Figures 3.5a and 3.8d, as well as the EG value of 3.58 eV corresponding to sample T45 a scheme was constructed which shows the levels where defects are located, see Figure 3.13 [8,26].

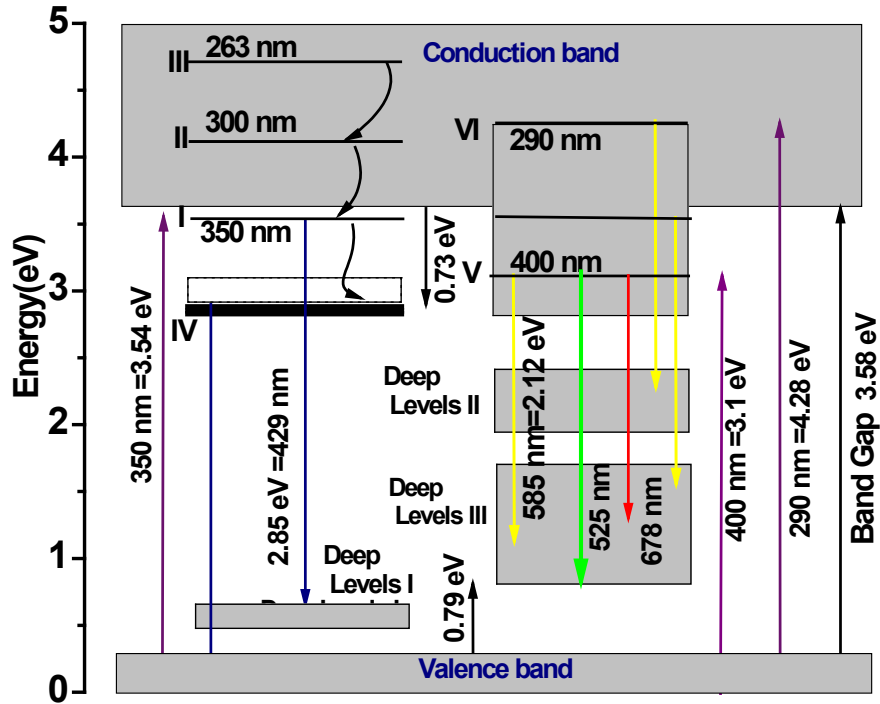


Figure 3.13: Proposed schematic showing the mechanisms of the blue and yellow emissions in ZnO quantum dots.

Samples T0-T4 emitting blue light only have defects centered at 263 nm, 300 nm, and 350 nm, then pump photons with an energy of 350 nm (3.54 eV) could excite electrons toward level I and those ones be relaxed radiatively reaching the deep level I or phononic relaxation may occur with the equivalent energy of 0.73 eV (2 phonons of OH groups) falling to the excited state IV, from which blue emission occur centered at 429 nm and electrons arrive to the valence band. The presence of OH according to FTIR of samples T1-T4 in Figure 3.4, could help to promote those non radiative relaxations. The same blue emission could be achieved by exciting with 300 nm (4.13 eV, level II) or 263 nm (4.71 eV, level III), but the blue emission is weaker than for an excitation at 350 nm because it would be more difficult to reach the level I or IV with phononic relaxations from II and III

and produce blue light. Taking as an example sample T3, we observed that the integrated emission by exciting at 300 nm is 83% of that obtained by exciting at 350 nm, this diminution in intensity could be associated to the fact that we need only 1.5 phonons to reach level I from II, but we need 3 phonons of OHs from level III to reach level I, thus blue emission is weaker exciting at 263 nm than for 300 nm. In fact, if we excite with energy below the band gap of T3 (3.76 eV), that is 400 nm or 3.1 eV, we did not observe blue emission, suggesting that we need at least 3.54 eV to reach defects emitting blue light, also non-radiative relaxations from the level V can not be possible to reach the level IV and produce blue light because there are not defects in that level V. In the case of the sample T0, see Figure 3.5a, lower energy (370 nm, 3.35 eV) could be used to excite such defects because the surface-bonded TEA states do not exist, thus, it is possible to associate the shifting in the excitation of defects from 370 nm to 350 nm to the interaction of amines coming from TEA with the surface of ZnO. Furthermore, Figure 3.13 shows the yellow-blue emission of sample T45 (EG=3.58 eV) under different excitation wavelengths with energies above the band gap (4.28 eV, level VI) or below the band gap (3.1 eV, level V). The highest intensity of yellow emission at 585 nm was obtained with excitation at 290 nm and the ratio of the integrated yellow/blue (Y/B) emission bands was 3.2, see Figure 3.8a, suggesting that yellow emission should be carried out from level VI to deep levels II mainly (the width of those levels is the difference in energy from 525 nm to 678 nm obtained from the FWHM of the broad yellow emission band), however some blue light emitting defects are also excited since those defects are in resonance with defects emitting yellow light, see the shoulder centered at 285 nm in the excitation spectra at 435 nm in Figure 3.8d. By decreasing the energy of excitation to 350 nm in level I, we observe that the yellow emission band dominates over the blue band again but the Y/B ratio increased to 4.1, suggesting that the amount of defects emitting blue light in level I is lower than for yellow emission again. If we continue decreasing the energy of excitation up to 400 nm, we observe that the Y/B ratio is 1.2, thus there are more defects for blue emission at level IV than in level I (the intensity of the yellow emission is

directly related with the amount of defects). It is worth to notice that levels IV and V are not in resonance, however the blue emission could be possible if the level I is extended above its “normal width” as illustrated by the shaded rectangle in Figure 3.13. In the case of samples T46-T48 which emitted white light due to the equilibrated emission of the blue and yellow light and excited at 350 nm, the amount of blue and yellow defects could be controlled with the volume of DCA since the intensity of the yellow and blue emissions changed according to the content of DCA, in fact the blue band is the most affected with the volume of DCA because the emission intensity of the blue band for a DCA volume of 0.45 ml. was lower than that for 0.17 ml. but in the case of the yellow emission the emission intensity for 0.45 ml. was higher than for 0.17 ml., those results suggests that the defects for blue emission are more sensible to DCA. In summary, most of the levels corresponding to defects emitting blue or yellow light are in resonance, as consequence, the intensity of the yellow or blue emission depends of the amount of defects in all levels, which can be controlled depending on the surfactant used (TEA or DCA) and the temperature of synthesis. Finally, based on results explained above, it is possible to say that we are exciting at the same time; zinc interstitial levels (I,II,II) which after transitions to the valence band or deep levels could produce blue emission and Oxygen vacancies levels (I,V,VI), whose transitions to deep levels II and III generate yellow light as explained by Zeng et al. [23].

3.5 ZnO based LEDs for white light generation

Two ZnO based LED devices were fabricated by spin coating, the configurations for those devices were: a) ITO/PEDOT (70 nm)/ TPD (50nm)/ZnO (T2, 130 nm)/Al (170 nm) (Device 1) and b) ITO/TPD (50nm)/PEDOT (70 nm)/ZnO (T3, 130 nm)/Al (170 nm) (Device 2), with an effective emitting area of 4 mm x 2mm. The results presented here resulted from averaging 4 samples for each type of device. The hole transport materials, poly(3,4-ethylenedioxythiophene) poly(styrenesulfonate) (PEDOT:PSS) and the N,N'-Bis(3-methylphenyl)-N,N'-

diphenylbenzidine (TPD) were acquired from Aldrich. Figure 3.14 shows the normalized electroluminescence spectra of devices 1 and 2 with CIE coordinate (0.31, 0.33) and (0.34, 0.37), respectively.

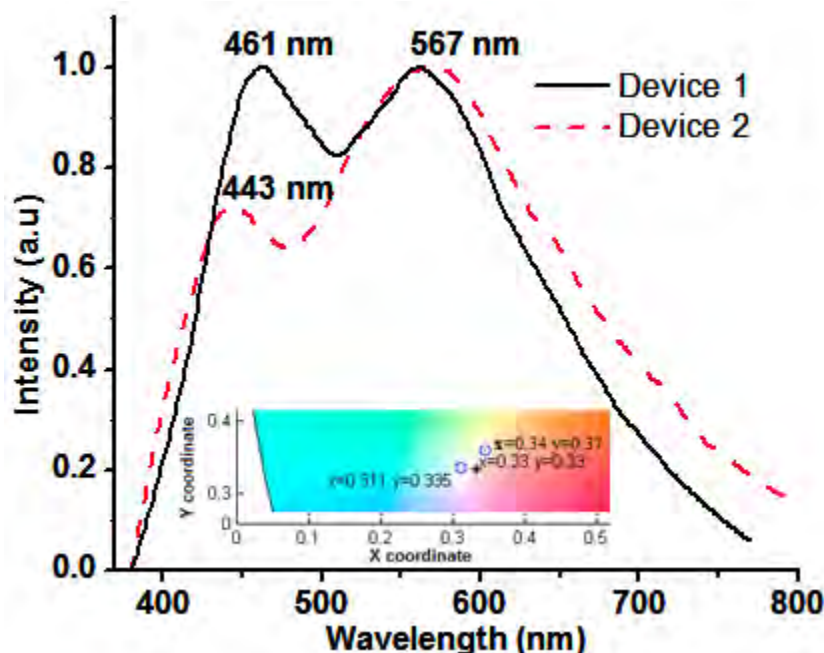


FIGURE 3.14: Electroluminescence spectra for the devices made with the sample T2 (device 1) and T3 (device 2), the inset shows the CIE coordinates for the emission of those devices.

The spectra were taken at 9 V and the turn on voltage was 4V for device 1 and 6V for device 2. The B/Y ratio (blue/yellow ratio resulted by dividing the integrated emission bands for blue and yellow light) was 0.61 and 0.28 for the device 1 and device 2, respectively. By comparing these ratios with the corresponding ones for photoluminescence spectra of samples T46-T48 (which emitted white light) in the Figure 3.12a, we observe an increase of 16% and 5% for the B/Y ratio, respectively.

The electrons trapped in defects after synthesis could be excited along with electrons injected after we apply voltage and then an increase in the B/Y ratio is possible, whereas in photoluminescence only electrons in defects are excited. This result suggests that a slight change in the shape of the emission spectra

can be expected in electroluminescence when ZnO nanoparticles are used as emissive layer (EML). Furthermore, a blue shift for the blue band from 435 nm in photoluminescence to 461 nm in electroluminescence as well as from 580 nm to 567 nm in the case of the yellow band is observed, see Figure 3.14. This shifting in the emission peaks as well as the broadening in the electroluminescence spectra from 750 to 800 nm (compare spectra in Figures 3.12a and 3.14) indicates that other type of defects are being excited when applying a forward bias. The emission observed in electroluminescence and photoluminescence are due to defects of ZnO because the electroluminescence emissions from TPD centered at 400 nm and 475 nm were not detected. Also, we did not detect the intrinsic UV electroluminescence of the ZnO gap located at 390 nm after electrical or optical injection. Moreover, the increase in the B/Y ratio and the shifting of the peaks in the electroluminescence bands could be associated to the way in which electrons trapped in defects are excited. In the case of photoluminescence, electrons are excited directly from traps, that is, from zinc interstitials and from interstitial oxygen for the blue emission and from oxygen vacancies for the yellow emission. In the case of electroluminescence, electrons are excited with voltage and they should arrive to the conduction band, from there, the electrons would be relaxed to fill the traps located inside the band gap for the ZnO. Then, the corresponding relaxations to the valence band and deep levels occur to produce blue and yellow emissions, see the band diagram in Figure 3.16. From this diagram, it is reasonable to assume that the zone for recombination and formation of excitons should be the interface between the TPD and ZnO layers. It would be easy to accumulate electrons coming from the Al electrode and holes arriving from PEDOT:PSS in this interface because the injection barrier height for electrons from Al to the conduction band of the ZnO is just 0.1 eV and the barrier to inject holes from the TPD to the valence band of ZnO is 1.9 eV. Figure 3.16 shows the I-V curves for the devices 1 and 2. In general, the density of current is higher for device 1, which had a more intense blue emission band than device 2, see Figure 3.14. Thus, this difference in

current could be assigned to the excitation of more defects which are emitting blue light. Therefore, the blue component was stronger for device 1.

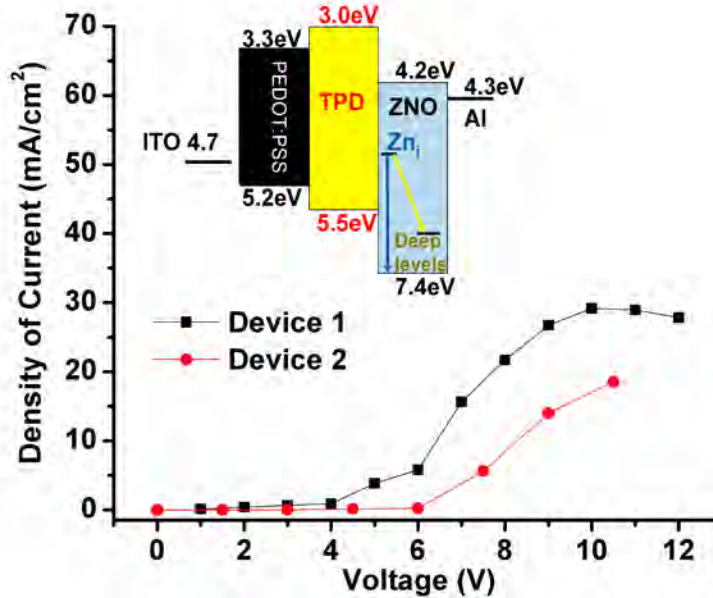


Figure 3.16: The I-V curves for devices 1 and 2, the inset is a band diagram for the ZnO based LEDs.

Moreover, the current for device 2 was lower probably because we have more DCA capping the nanoparticles in this device in comparison to device 1. As a consequence, it is expected to need more voltage for the electrons to arrive to the defects and to give out light in device 2, this fact is reflected in the turn on voltage, since it was 4V and 6V for devices 1 and 2 respectively. Finally, it is noticeable that the maximum current consumption at 10V was 2.32 mA and 1.66 mA for the devices 1 and 2 respectively, which is lower or comparable to those currents reported for ZnO based LEDs [24,27].

3.6 Conclusions for chapter 3

A change in morphology of ZnO nanoparticles from spherical quantum dots to nanorods according to the type of surfactant (TEA or DCA) or temperature used during synthesis was demonstrated. In addition, the intensity of blue emission in ZnO quantum dots could be controlled according to the volume of TEA. It was observed that the presence of ammine as well as of OH groups, have an important role in increasing or decreasing the surface states or Zn interstitials that produce blue emission. Also, the energy band gap values (EG) and the size of ZnO quantum dots were controlled by the volume of TEA. Two methods were used to calculate this band gap and the maximum difference in the values of EG by using both methods was 7%. On the other hand, the yellow emission from ZnO quantum dots was originated from oxygen vacancies and that an increase in size and conglomeration are important to get this type of defects. When TEA was changed by Dodecylamine, ZnO nanorods with an average length of 160 nm were obtained and those nanoparticles contained defects that emitted blue and yellow light. Finally, ZnO based LEDs were fabricated, those devices had CIE coordinates of (0.31, 0.33) which is near the ideal white light coordinates of (0.33, 0.33), suggesting that they could be useful for applications in displays and lighting. Optimization of those LEDs is needed to increase lifetime and brightness and to be commercially competitive.

References Chapter 3

- [1] A. Goldeblum, A. Belum-Marian, and V. Teodorescu, J. of Opt. and Adv. Mat. 8, 2129 (2006)
- [2] Z.W. Donga, C.F. Zhang, H. Deng, G.J. You, and S.X. Qian, Mat. Chemis. and Phys. 99, 160 (2006).
- [3] J. W. P. Hsu, D. R. Tallant, R. L. Simpson, N. A. Missert, and R. G. Copeland, Appl. Phys. Lett 88, 252103 (2006)
- [4] H. L. Cao, X. F. Qian, Q. Gong, W. M. Du, X. D. Ma, Z. K. Zhu Nanotechnology 17, 3632 (2006).
- [5] M.A. Bakar, M.A.A. Hamid and A. Jalar Adv. Mat. Res. 97-101, 1550 (2010).
- [6] M.S. Mamat, Z. Khusaimi, and M.R. Mahamood, Defect and Difusion forum 312-315, 116 (2011)
- [7] N. Rajeswari Yogamalar, R. Srinivasan, and A. Chandra Bose, Opt. Mat. 31, 1570 (2009).
- [8] Y.S. Fu, X.W. Du, S.A. Kulinich, J.S. Qiu, W.J. Qin, R. Li, J. Sun, and J. Liu, J. Am. Chem. Soc. 129, 16029 (2007).
- [9] K. Thongsuriwong, P.Amorntitoksuk, and S.Suwanboon, J. of Phys. and Chem. of Solids 71, 730(2010).
- [10] Y. Gu, Igor L. Kuskovsky, M. Yin, S. O'Brien, and G. F. Neumark, Appl. Phys. Lett. 85, 3833 (2004).
- [11] Cheng-Hsien Hsieh, J. of the Chin. Chem. Soc, 54, 31(2007)

- [12] M. Vafaei, and M. Sasani Ghamsari, *Materials Letters* 61, 3265 (2007).
- [13] D. Sun, M. Wong, L. Sun, Y. Li, N. Miyatake, and H.J. Sue, *J. Sol-Gel Sci. Technol.* 43, 237 (2007).
- [14] M.L. Singla, M. Shafeeq, and M. Manish Kumar, *J. of Lumines.* 129, 434 (2009).
- [15] Z. Fang, Y. Wang, D. Xu, Y. Tan, and X. Liu, *Opt. Mat.* 26, 239 (2004).
- [16] M.K. Patra, M. Manoth, V.K. Singh, G. Siddaramana Gowd, V.S. Choudhry, S.R. Vadera, and N. Kumar, *J. of Lumin.* 129 320 (2009).
- [17] L. Iriraman, V. P. N. Nampoory, P. Radhakrishnan, A. Deepthy, and Bindu Krishnan, *J. Appl. Phys.* 102, 063524 (2007)
- [18] G. Kiliani, R. Schneider, D. Litvinov, D. Gerthsen, M. Fonin, U. Rudiger, A. Leitenstorfer, and Rudolf Bratschitsch, *Opt. Expr.* 19, 1641 (2011)
- [19] S. KUMAR and P. D. SAHARE, *NANO: Brief Reports and Reviews* 7, 1250022 (2012)
- [20] Z.W. Donga, C.F. Zhang, H. Deng, G.J. You, and S.X. Qian, *Mat. Chemis. and Phys.* 99, 160 (2006).
- [21] Cheng-An J. Lin, Ting-Ya Yang, Chih-Hsien Lee, Sherry H. Huang, Ralph A. Sperling, Marco Zanella, Jimmy K. Li, Ji-Lin Shen, Hsueh-Hsiao Wang, Hung-I Yeh, Wolfgang J. Parak and Walter H. Chang, *ACS Nano* 3, 395 (2009).
- [22] Y. H. Shin and M. D. Kim, *J. of the Kor. Phys. Soc.* 53, 2504 (2008)
- [23] H. Zeng, G. Duan, Y. Li, S. Yang, X. Xu, and W. Cai, *Adv. Funct. Mater.* 20, 561 (2010).

[24] Y. He, J. A. Wang, X. B. Chen, W. F. Zhang, X. Y. Zeng, and Q. W. Gu, J. Nanopart. Res. 12, 169 (2009).

[25] D. Haranath, S. Sahai, A. G. Joshi, B.K. Gupta, and V. Shanker, Nanotechnology 20, 425701 (2009)

[26] A. A. Sokol, S. A. French, T. S. T. Bromley, C. Richard, A. Catlow, H. J. J. van Dame and P. Sherwoode, Faraday Discuss. 134, 267 (2007).

[27] C. Y. Lee, J. Y. Wang, Y. Chou, C. L. Cheng, C. H. Chao, S. C. Shiu, S. C. Hung, J. J. Chao, M. Y. Liu, W. F. Su, Y. F. Chen and C. F. Lin, Nanotechnology 20, 425202 (2009).

Chapter 4

White light generation from YAG/YAM: Ce³⁺ and YAG/YAM: Ce³⁺,Pr³⁺,Cr³⁺ nanophosphors by photoluminescence and electroluminescence

4.0 Introduction

In this chapter, the effect of Ammonia (NH₄OH) on the luminescent properties of YAG/YAM:Ce³⁺,Pr³⁺,Cr³⁺ under the excitation wavelengths of 340 nm and 460 nm is analyzed. YAG is yttrium aluminum garnet and YAM yttrium aluminum monoclinic. The goals of this part of the thesis were: 1) to understand how the introduction of ammonia could increase the red component of the overall emission in YAG/YAM:Ce³⁺,Pr³⁺,Cr³⁺ nanophosphors when excited with 460 nm; 2) to study the emission of a broad red band of Pr³⁺ superposed to the yellow emission of Ce³⁺ when the YAG/YAM:Ce³⁺,Pr³⁺,Cr³⁺ nanophosphors are excited at 340 nm; and 3) to explain white light emission with CIE coordinates (0.30,0.36) produced by the overlapping of the yellow-red light of the YAG/YAM:Ce³⁺,Pr³⁺,Cr³⁺ nanophosphors and the blue light of a dye under excitation at 340 nm. In addition, a blue emitting OLED made with poly[(9,9-dioctylfluorenyl-2,7-diyl)-co-(4,4'-(N-(4-sec-butylphenyl)) iphenylamine)] (TFB) which had YAG/YAM:Ce³⁺ incorporated on it was fabricated. By exciting the doped YAG/YAM with the blue light coming from the OLED, white light with a CIE coordinate of (0.31,0.32) was obtained.

4.1 Synthesis and characterization of YAG/YAM: Ce³⁺ and YAG/YAM: Ce³⁺,Pr³⁺,Cr³⁺ nanophosphors

All the chemical precursors, Y(NO₃)₃·5H₂O, Al(NO₃)₃·5H₂O, Ce(NO₃)₃·5H₂O, Pr(NO₃)₃·5H₂O and cetyltrimethylammonium bromide (CTAB), were acquired from Aldrich Inc. and ammonia (NH₄OH) was purchased from Karal, all precursors were used without further treatment. The YAG/YAM:Ce³⁺,Pr³⁺ and

YAG/YAM:Ce³⁺ nanophosphors co-doped with 0.1 mol% of Ce₂O₃ and 0.1 mol% of Pr₂O₃, were synthesized by an hydrothermal process. Fourteen samples were prepared using sodium hydroxide (NaOH) as precipitant agents and ammonia (NH₄OH) was added to six of them. In this procedure, all nitrates and CTAB (5 wt%), were mixed in distilled water at room temperature under vigorous stirring, subsequently, the precipitation was achieved with a solution (4M) of sodium hydroxide added by slow dropping. Ammonia was added after the solution of NaOH. Thereafter, the resulting solution was transferred into a sealed autoclave, which was maintained at 100 °C during 12 h. The precipitate was washed with distilled water and ethanol several times and dried in an oven at 100 °C for 12 h. Finally, the samples were annealed at 900°C and 1100°C for 3 h, with a heating rate of 5°C /min. Table 4.1 summarizes the composition and main parameters of synthesis of the fourteen samples. (-) means that the corresponding parameter in the column was not employed during the synthesis procedure. Samples C1 and C2 were obtained by impregnating the sample N1 with coumarin 480 as explained in section 4.1.1.

Table 4.1: Synthesis' parameters of YAG/YAM:Ce³⁺,Pr³⁺,Cr³⁺ nanophosphors.

Sample	Ce ³⁺ (%mol)	Pr ³⁺ (%mol)	Cr ³⁺ (%mol)	Ammonia (ml.)	Annealing Temperature (0C)	Dye (mgr.)
N1	0.1	0.1	Traces	-	900	-
N2	0.1	0.1	Traces	25	900	-
N3	0.1	0.1	Traces	-	1100	-
N4	0.1	0.1	Traces	25	1100	-
C1	0.1	0.1	Traces	-	900	0.6
C2	0.1	0.1	Traces	-	900	1.0
N11	0.1	-	Traces	-	900	-
N12	-	0.1	Traces	-	900	-
N21	0.1	-	Traces	25	900	-
N22	-	0.1	Traces	25	900	-
N31	0.1	-	Traces	-	1100	-
N32	-	0.1	Traces	-	1100	-
N41	0.1	-		25	1100	-
N42	-	0.1		25	1100	-

It is worthy to mention that during the synthesis of YAG/YAM:Ce³⁺, Pr³⁺ trace impurities of Cr³⁺ appeared. Those impurities came from the corrosion of the stainless autoclave used for synthesis, since the pH used for synthesis after adding Ammonia was 12, which is able to produce degradation of the stainless autoclave. It was not possible to detect those trace impurities using conventional methods as explained later.

4.1.1. Blue dye-impregnating procedure

The Sample N1 annealed at 900⁰C which presented the broadest visible emission under 340 nm excitation, was impregnated with the efficient blue dye Coumarin 480 in the following way: 0.6 mg of that dye were dissolved on 20 ml of

absolute ethanol, then, 100 mg of the N1 sample were introduced in 10 ml. of the solution and a strong stirring was carried out during 1 hr. Afterwards, that solution was dried at 100°C during 1 h, and the resulting powder was recuperated to make a pellet (Sample C1). A similar procedure was used to obtain another dye-impregnated YAG/YAM sample, but the initial solution was 1 mg of Coumarin in 20 ml. of absolute ethanol (Sample C2).

4.1.2 Structural and morphological characterization

The characteristic XRD patterns of the prepared samples are shown in Figure 4.1. Such patterns show a mixture of cubic phase of YAG and monoclinic phase of YAM for samples annealed at 900 °C, according to JCPDS 33-0040 (YAG) and JCPDS 83-0935 (YAM) cards. The phase composition was estimated by the Rietveld iterative process [1].

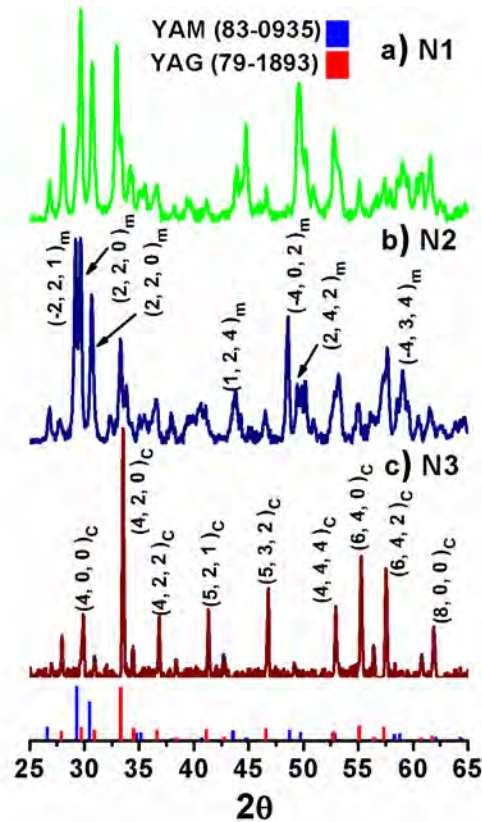


Figure 4.1: XRD of nanopowder annealed at 900 °C and synthesized with, a) NaOH (N1), b) NaOH+NH₄OH (N2), c) NaOH annealed at 1100 °C (N3).

The phase composition was (YAG/YAM) 55/45 wt% and 63/37 wt% for samples prepared without (N1) and with (N2) *ammonia*, respectively, see figure 4.1a,b. The increment of annealing temperature to 1100 °C stabilizes completely (100 wt%) the YAG crystalline phase for both N3 and N4 prepared samples as is described in figure 4.1c. Then, it is reasonable to conclude that the introduction of ammonia helps to stabilize the YAG crystalline phase at 900°C. In addition, N11 and N12 has the same phase composition than N1, while N21 and N22 have the same composition than N2. This suggests that the content of dopant is not influencing the phase composition. Same situation was observed for N31 and N32 as well as for N41 and N42, where their phase composition is similar to N3 and N4 respectively. YAG is a cubic phase with space group Ia₃d and cell parameter $a = 12.01\text{\AA}$, while YAM is monoclinic with space group P2₁/c and $a = 0.7373\text{nm}$, $b = 1.0467\text{nm}$, $c = 1.1121\text{nm}$, and $\beta = 108.53^\circ$ [2]. YAG presents dodecahedral, octahedral and tetrahedral sites, named A, B and C sites respectively. In this garnet, Y⁺ occupies the A site, therefore Pr³⁺ could take this place [3]. In the case of YAM, the Y⁺ ion could be coordinated to six or seven oxygen atoms, thus, Pr³⁺ could occupy a six-coordinated center or seven-coordinated center. According to HRTEM images, the average particle size of N1 and N2 are 50 nm, see Figure 4.2.

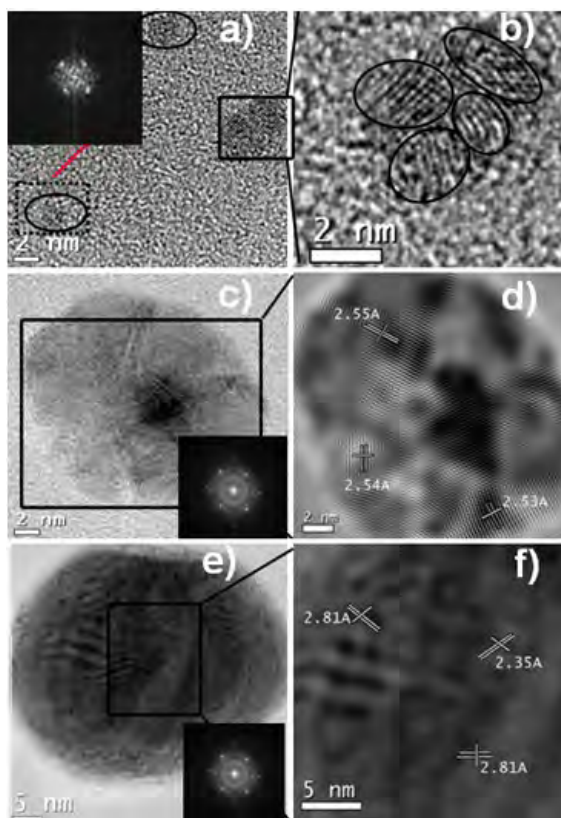


Figure 4.2: Typical TEM and HRTEM images of sample N1 showing the seeds nanocrystals a) and its agglomeration b), which grow to form a larger particle c) with HRTEM image showing the interplanar distance d). e) and f) correspond to a particle formed with an ensemble of polycrystals and the HRTEM showing a distorted interplanar distance. The insets show the fast fourier transform (FFT) pattern for each stage of growing.

A careful analysis of HRTEM images suggests that such nanoparticles are the result of the agglomeration of small nanocrystals as described in figure 4.2 for N1 samples, although a similar behavior was observed for N2. The growth mechanism of these nanoparticles is as follow. At first stage of the synthesis, nanoparticles of 2 nm were obtained as is shown in Figure 4.2a, the inset display the Fast Fourier Transform (FFT) showing the crystalline nature. These nanocrystals act as seeds which, on time, self assemble to form an irregular agglomerate of nanocrystals as is clearly observed on figure 4.2b. Such nucleation grow with time in a disordered manner to form bigger polycrystalline

particles, figure 4.2c shows nanoparticles with a size of 11 nm approximately. The inset shows the FFT confirming the crystalline nature of the particle. Furthermore, the HRTEM image from figure 4.2c is displayed in figure 4.2d, and an interplanar separation of 2,54 Å was measured. Those polycrystalline particles keep nucleation growing to form a final polycrystalline nanoparticle of 50 nm, see figure 4.2e. In this case, the HRTEM image shows an interplanar separation of 2.81 Å, see figure 4.2f. Such distortion is probably associated to the irregular aggregation of nanocrystals [4,5].

4.2 Impurities

The FTIR spectra of samples N1, N2, N3 and N4 in Figures 4.3a,b depict a sharp band centered at 479 cm^{-1} which is attributed to the stretching vibrations of the AlO_4 tetrahedra, as well as two bands peaking at 732 cm^{-1} and 798 cm^{-1} which are associated to stretching vibration of the AlO_6 octahedra [6]. Also the peaks at 1016 cm^{-1} , 1464 cm^{-1} , and the band around 3474 cm^{-1} are attributed to CO_2 groups, bending vibration of OH groups from the residual adsorbed water, and stretching vibration of OH groups adsorbed on the surface of YAG nanophosphors, respectively [6,7]. Moreover, Y-O vibrations correspond to the 460 cm^{-1} and 560 cm^{-1} bands [8]. By comparing the samples N1 and N2 annealed at 900°C , it is noticeable that the amount of OH groups and CO_2 impurities did not change, indicating that the introduction of ammonia does not have an effect over the content of impurities on YAG/YAM: Ce^{3+} , Pr^{3+} , Cr^{3+} nanocrystals.

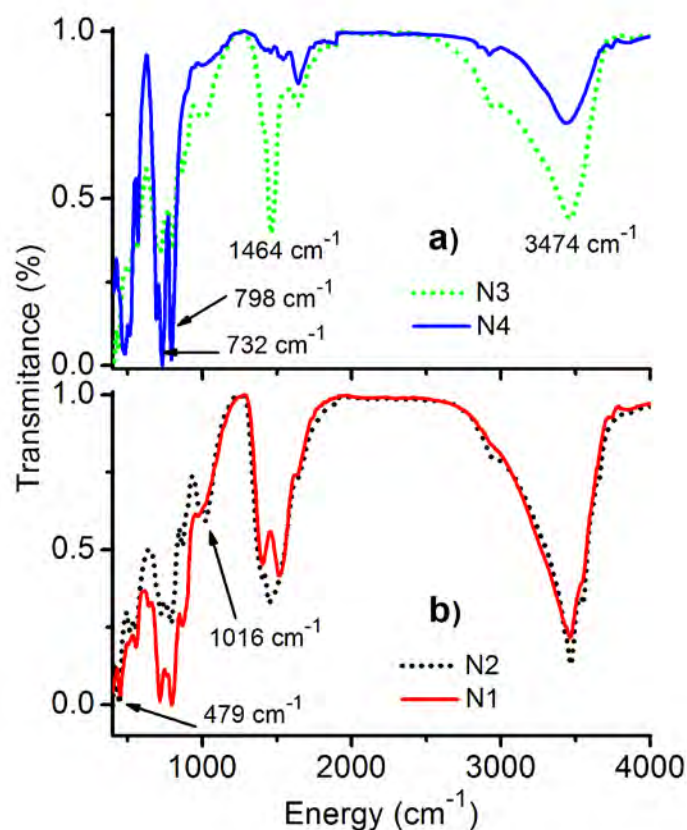


Figure 4.3: FTIR spectra of a) N1 and N2 samples annealed at 900°C; b) N3 and N4 samples annealed at 1100°C.

Interestingly, the presence of ammonia enhances the absorption of bands associated to AlO_6 octahedra but do not affect the one associated to tetrahedra AlO_4 . Furthermore, a direct comparison between samples N1 and N3 suggests that the increment of annealing temperature reduces impurities, but the combined effect with the presence of ammonia reduces strongly the OH content. Furthermore, the combined effect strongly enhances the absorption bands of both tetrahedral and octahedral suggesting that combined ammonia and higher annealing temperature contribute to a better binding between Al and O_2 atoms. In this way, a minimum of impurities and a pure YAG phase can be reached at lower temperatures than those employed in other methods such as solid-state reaction [9].

4.3 Optical Properties

4.3.1 Fluorescent properties of YAG/YAM:Ce³⁺,Pr³⁺,Cr³⁺ under 460 nm excitation

The signal emitted by YAG/YAM:Ce³⁺,Pr³⁺,Cr³⁺ nanophosphors after excitation at 460 nm is displayed in figure 4.4. The spectra on panel a) present a strong orange emission peak centered at 609 nm associated to the transition $^1D_2 \rightarrow ^3H_4$, and very weak bands at 640 nm and 670 nm may be associated to $^3P_0 \rightarrow ^3H_6$ and $^3P_0 \rightarrow ^3F_2$ transitions of Pr³⁺, overlapped with the strong green-yellow emission of Ce³⁺ associated to the transition $5d \rightarrow ^2F_{5/2}, ^2F_{7/2}$. Such emissions are in agreement with the results reported by other authors [10-12].

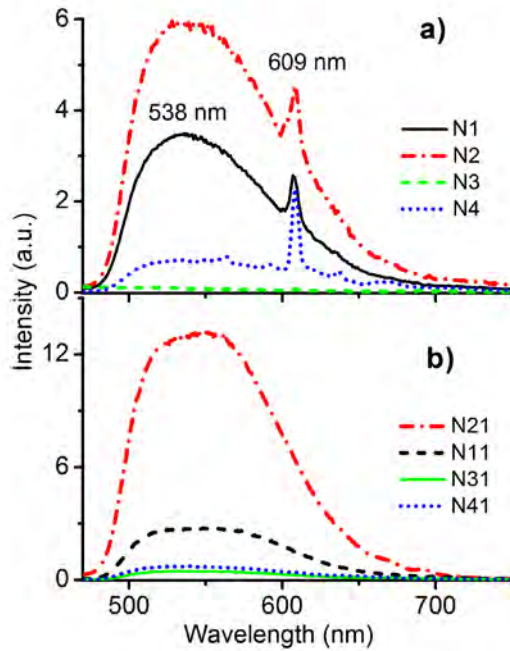


Figure 4.4: Photoluminescence of a) codoped Ce³⁺,Pr³⁺ and b) doped Ce³⁺, both under 460 nm excitation.

Notice the strong increment of 83% in the integrated emission band (by comparing samples N1 and N 2), see figure 4.4a, which could be partially associated with the stabilization of YAG crystalline phase changing from 55 wt%

to 63 wt% as a result of the introduction of ammonia and annealing at 900 °C as was discussed above. However, strong quenching of both Ce^{3+} and Pr^{3+} emission was observed for samples N3 and N4 regardless of the 100 wt% of YAG crystalline phase. Furthermore, quenching of the Ce^{3+} emission is also observed even in the absence of Pr^{3+} , see figure 4.4b. In this case, a larger enhancement in red emission with the introduction of ammonia occurred (except for samples annealed at 1100 °C), while the small quenching at high annealing temperature suggests that the phenomena associated to quenching effect depends on both active ions.

The luminescence quenching observed experimentally can be explained by the formation of Pr^{4+} and Ce^{4+} . As has been reported, Pr^{4+} ions are detrimental for the fluorescence emission because they promote the formation of F color centers which act as a trap for electrons [12]. Those color centers are formed when the oxidation from Pr^{3+} to Pr^{4+} liberates an electron which is trapped in anionic vacancies; this in turn induces a charge compensation producing oxygen defects V_O . The experimental evidence of the formation of Pr^{4+} on samples N3 and N4 annealed at 1100 °C is based on the brown coloration of the samples that has been reported by other authors [13]. In addition, those samples presented broader absorption bands in comparison to samples annealed at 900 °C (N1 and N2), due to the superposition of F color centers, oxygen vacancies in the range of 500-700 nm and Pr^{4+} in the range of 300-570 nm as displayed in Figure 4.5 [12,14,15]. Furthermore, absorption spectra suggest that high annealing temperature promote the formation of Pr^{4+} but the presence of ammonia prevents it. This can be corroborated observing that sample N2 has a lower Pr^{4+} absorption band than sample N1 and also has a higher Pr^{3+} absorption band centered at 254 nm, see Figure 4.5 [12]. A similar increment on such absorption band was also observed for sample N4 annealed at 1100 °C. Thus, Pr^{4+} is formed in all samples under study perhaps due to the specific characteristics of the synthesis process, combined with the oxidative atmosphere

where samples were annealed, promoted for a high annealing temperature, and avoided with the presence of ammonia.

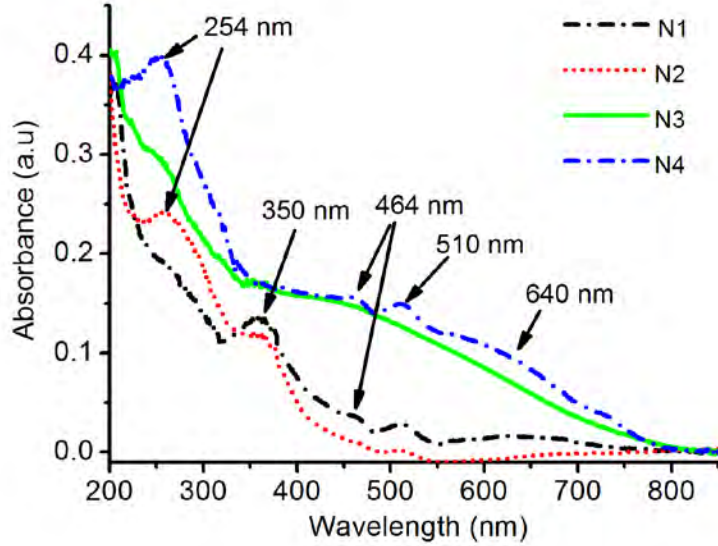


Figure 4.5: Absorption spectra of YAG/YAM:Ce³⁺,Pr³⁺,Cr³⁺ nanophosphor.

Absorption bands at 254 nm and 640 nm related to Pr³⁺ [12], and bands at 464 nm and 510 nm associated to Ce³⁺ disappeared for N3 but remain for N4, as is also shown in Figure 4.5. This suggests the oxidation of Ce³⁺ to Ce⁴⁺ which is possible because the annealing was performed in an oxidizing environment. Such oxidation could partly explain the quenching of the signal emitted by Ce³⁺ in all samples, see figure 4.4a, and was confirmed by the emission spectra of YAG/YAM:Ce³⁺ shown in figure 4.4b. In this case, samples were prepared similarly than those shown in figure 4.4a except that no Pr³⁺ was included. As observed, the emission of Ce³⁺ is quenched after annealing at 1100 °C, indicating the presence of oxidation from Ce³⁺ to Ce⁴⁺. Notice the similar signal emitted for N31 and N41, and the large increment with the presence of ammonia. In order to understand the emission mechanism under 460 nm excitation, a YAG/YAM:Pr³⁺ (N22) sample was prepared by using the same synthesis procedure that for N2, except that Ce³⁺ was not included. Figure 4.6a displays the excitation spectrum at $\lambda_{emis} = 609nm$ for the N22. Three Pr³⁺ excitation bands

centered at 237 nm, 257 nm and 290 nm are associated to $^3H_4 \rightarrow 4f^15d$ transitions, and multiple peaks around 460 nm associated to $^3H_4 \rightarrow ^3P_j$ transition were observed.

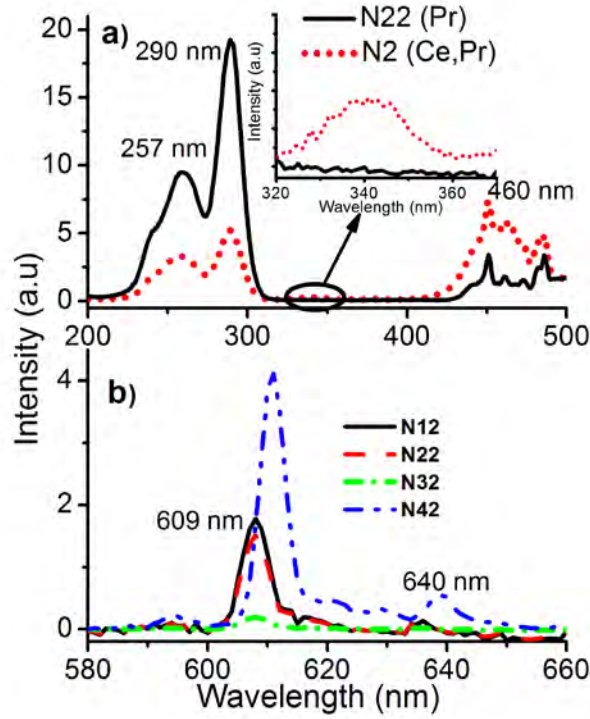


Figure 4.6: a) Excitation spectra of Pr³⁺ doped and Ce³⁺,Pr³⁺ codoped at $\lambda_{emi}=609$ nm. The inset shows a close up of the marked area. b) Photoluminescence of Pr³⁺ doped samples under 460 nm excitation.

With the introduction of Ce³⁺ (N2), the excitation spectrum of YAG/YAM:Ce³⁺,Pr³⁺Cr³⁺ at 609 nm shows broader 460 nm band due to the higher absorption cross section for Ce³⁺ and associated to the transition $^2F_{5/2} \rightarrow ^5d_1$ overlapped with peaks associated to $^3H_4 \rightarrow ^3P_j$ transition of Pr³⁺. An additional weak band centered at 340 nm associated to the second 5d level (5d₂) transition of Ce³⁺ was also observed [16]. Notice that both ions can be excited at 460 nm for 609 nm emission, but only with the presence of Ce³⁺ can be obtained such emission under excitation at 340 nm. Therefore, it is reasonable to conclude

that 609 emission band of Pr^{3+} is the result of both direct and energy transfer from Ce^{3+} at 460 nm excitation, see figure 4.6b. In the former (direct excitation), $^1\text{I}_6$ is populated after excitation and then relaxed non-radiatively to $^1\text{D}_2$ that relaxes radiatively producing 609 nm ($^1\text{D}_2 \rightarrow ^3\text{H}_4$), and radiative relaxation producing 640 may be associated to $^3\text{P}_0 \rightarrow ^3\text{H}_6$ transition or associated to non-radiative relaxation followed by radiative relaxation to ground state ($^1\text{D}_2 \rightarrow \Delta E_{\text{phon}} + ^3\text{H}_4$). Although the absence of the well-known emission band at 490 nm ($^3\text{P}_0 \rightarrow ^3\text{H}_4$) can be explained by the re-absorption for Ce^{3+} in the codoped system, only a weak signal was observed in the Pr^{3+} doped samples suggesting that the presence of defects quenches such emission. It has been postulated that quenching of 490 nm emission, and any other band associated to $^3\text{P}_0$ relaxation, is possible with the presence of intervalance charge transfer (IVCT) band located between $^3\text{P}_0$ and $^1\text{D}_2$ levels [17-19]. Such band could be composed of color centers or defects produced by charge compensation during the oxidation of Ce^{3+} , Pr^{3+} to Ce^{4+} , Pr^{4+} , or during the synthesis process. In this case, relaxation of population follow the scheme $^3\text{P}_0 \rightarrow \text{IVCTB} \rightarrow ^1\text{D}_2$, which explain why the dominant emission band is coming from $^1\text{D}_2$ energy level and only small population from $^3\text{P}_0$ relaxes radiatively to the ground state. Furthermore, the presence of such defects also suggest that 640 and 670 nm emission bands should be associated to non-radiative relaxation of $^1\text{D}_2$ to some defects and then the radiative relaxation to the ground state as will be discussed later. Transitions discussed above are displayed in the energy diagram of figure 4.7, and are in correspondence with previous results reported in the literature [3,11,12,14,20].

In the energy transfer mechanism, Pr^{3+} can be excited either by a non-radiative energy transfer from the lowest part of 5d levels ($^2\text{D}_{3/2}$) of Ce^{3+} to $^1\text{I}_6$ of Pr^{3+} (ET₁) or by a radiative energy transfer from relaxed 5d of Ce^{3+} to $^1\text{D}_2$ of Pr^{3+} (ET₂) as described in figure 4.7. From those excited levels, the relaxation mechanism is similar as described above producing the 609 nm dominant band from Pr^{3+} . Thus, the energy transfer mechanisms and direct excitation occur at the same time. This explains the enhancement emission of Pr^{3+} , even though the emission

of Ce^{3+} dominates the emitted signal; see emission of N1 and N2 in Figure 4.4a. Therefore, considering the excitation band at 340 nm for Ce^{3+} and the possibility to excite Pr^{3+} by energy transfer, it should be possible to get both yellow emission from Ce^{3+} and red emission from Pr^{3+} by exciting at 340 nm as will be discussed in the next section.

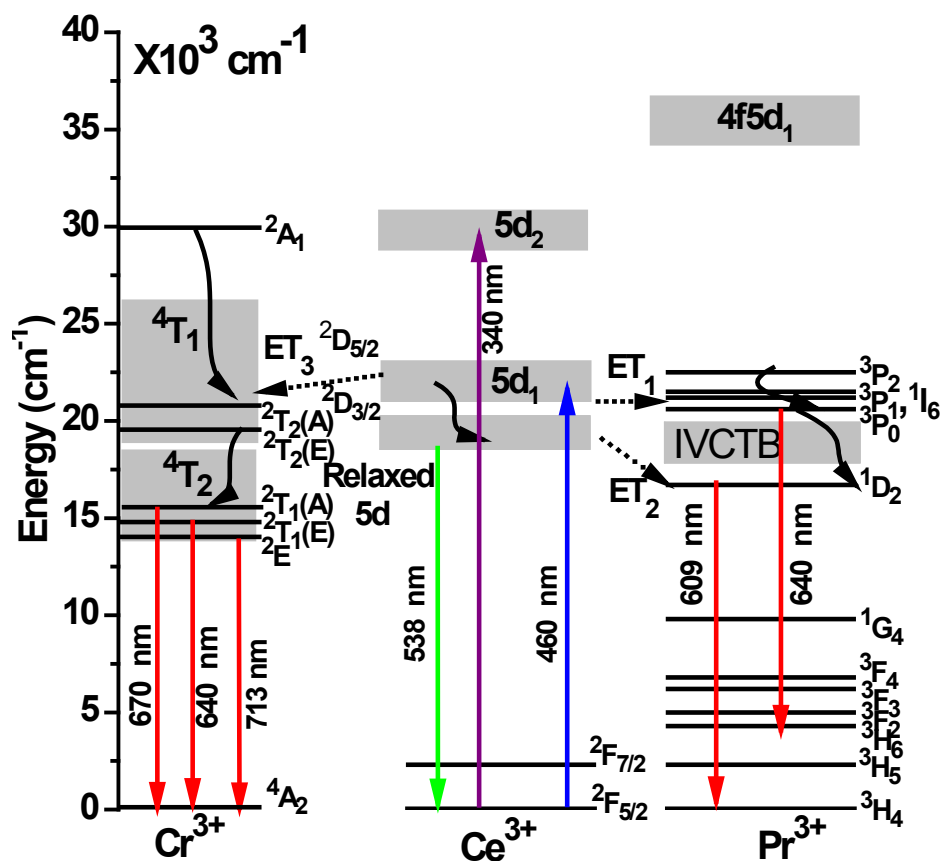


Figure 4.7: Energy level diagram with the proposed mechanism of Ce^{3+} , Cr^{3+} and Pr^{3+} emission.

4.3.2 The fluorescent properties of $\text{YAG/YAM}:\text{Ce}^{3+}, \text{Pr}^{3+}, \text{Cr}^{3+}$ under 340 nm excitation

Dominant broad red emission overlapped with the yellow emission of Ce^{3+} were observed in samples N1-N4 after excitation at 340 nm as is displayed in figure 4.8a. Interestingly, the red band is not dominated by the typical 609 nm emission associated to $^1\text{D}_2 \rightarrow ^3\text{H}_4$ transition of Pr^{3+} as discussed above and only a weak

signal of such band can be observed in the emission spectra. However, its presence confirms the energy transfer $\text{Ce}^{3+} \rightarrow \text{Pr}^{3+}$. The dominant band centered at 670 nm cannot be associated to $^3\text{P}_0 \rightarrow ^3\text{F}_2$ or $^1\text{D}_2 \rightarrow ^3\text{H}_5$ because this would require population of $^3\text{P}_0$ and $^1\text{D}_2$ that in turn should dominate the signal emitted after radiative relaxation, as discussed above. In addition, the same spectra were obtained in the absence of Ce^{3+} (or Pr^{3+}) as is displayed in figure 4.8b suggesting that such radiative relaxation should be associated to some impurities introduced during the synthesis process.

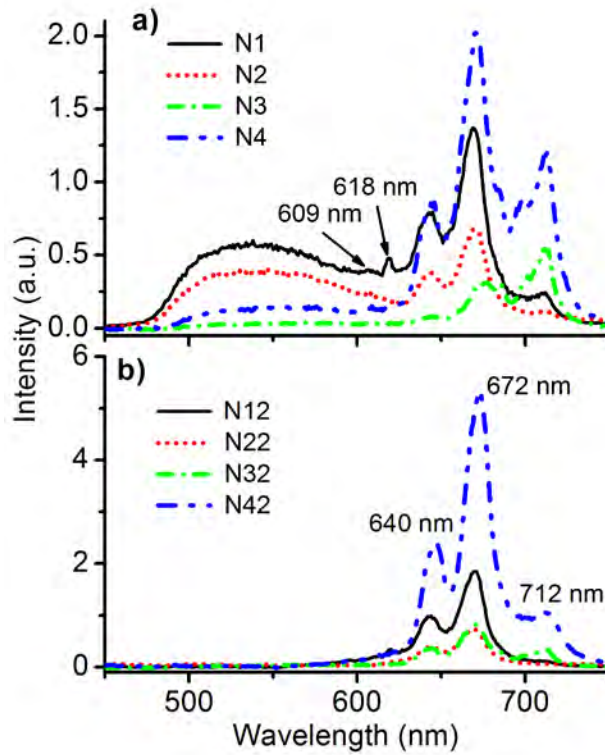


Figure 4.8: Photoluminescence of a) codoped $\text{Ce}^{3+}, \text{Pr}^{3+}$ and b) doped Pr^{3+} , both under 340 nm excitation.

Recently, the red emission of Ce^{3+} can be enriched by codoping with Cr^{3+} with dominant emission bands peaking at 670, 685 and 700 nm [22] was reported. Those bands are in agreement with those bands observed in our experiments, see figure 4.8a, and therefore they confirm the presence of Cr^{3+} impurities in our

nanophosphors. Such impurities must be in the level of traces because they were not detected by EDS analysis. In our case, impurities came from the autoclave used for the preparation of nanocrystals as was confirmed by the preparation in a different container. The proposed mechanism for the excitation and relaxation of Cr^{3+} is displayed in figure 4.7 and it can be described as follows: Although Cr^{3+} can be excited directly to $^2\text{A}_1$ energy band, it is possible that after excitation at 340 nm the $^5\text{d}_2$ level of Ce^{3+} was populated and partially relaxed non-radiatively to $^5\text{d}_1$ that in turn relaxes to ground state radiatively producing the yellow band centered at 560 nm. In addition, a non-radiative decay can occur from the $^5\text{d}_1$ band of Ce^{3+} to $^4\text{T}_1$ and $^2\text{T}_2(\text{E})$ energy bands of Cr^{3+} (ET_3) and then to $^4\text{T}_2$, $^2\text{T}_1(\text{A})$, $^2\text{T}_1(\text{E})$ and 2E that relaxes to ground state $^4\text{A}_2$ producing the red emission band, see figure 4.7. Notice that the energy transfer from $^5\text{d}_1$ (Ce^{3+}) to $^2\text{T}_2(\text{E})$ (Cr^{3+}) after excitation of 460 nm is also possible. Although the explanation of 672 nm dominant band is consistent with the experimental results, more studies are in progress to confirm the proposed mechanism that will be reported in a forthcoming paper.

The signal emitted is dominated by the red band but the yellow to red ratio (Y/R) was changed with the introduction of ammonia and the increment of annealing temperature. The Y/R for N1 was ~ 0.42 and changes to ~ 0.007 for N3 as a consequence of the complete stabilization of the YAG crystalline phase. In this last case, the signal emitted is dominated by the red band, in contrast excitation at 460 nm where signal emitted of N3 disappears. As was observed previously, the introduction of ammonia enhances the red emission of Pr^{3+} under excitation at 340 nm as observed by comparing the ratio $\text{Y/R} \sim 0.59$ for N2 and $\text{Y/R} \sim 0.07$ for N4. Notice the strong enhancement of 670 nm emission band with the combined effect of ammonia and pure YAG crystalline phase. These experimental results confirm the important role of the ammonia and YAG/YAM phase composition. It suggests that Pr^{3+} emission is enhanced by YAG crystalline phase and that the presence of ammonia reduces the formation of Pr^{4+} . This conclusion can be extended to Ce^{3+} if we assume that the presence of ammonia does not favor the

reduction of Ce^{4+} . It is important to note that adequate balance between yellow and red emission was obtained for N1 and N2 where YAM crystalline phase is present.

Interestingly, the contribution of red emission under UV excitation can be controlled either by the addition of ammonia or annealing temperature as is shown in figure 4.8a. This suggests that $\text{YAG}:\text{Ce}^{3+}, \text{Pr}^{3+}, \text{Cr}^{3+}$ nanophosphors could be excellent candidates to generate white light under 340 nm excitation. As a proof of concept, a blue component was added and white light was obtained as is discussed in the next section.

4.4 White light emission in photoluminescence under 340 nm excitation

Several groups have reported very efficient LEDs emitting in the ultraviolet region at 340 nm for the study of organic molecules, biosensing applications and solid-state lighting [21-24]. For lighting applications, RGB phosphors are required, therefore the yellow-red emission of $\text{YAG/YAM}:\text{Ce}^{3+}, \text{Pr}^{3+}, \text{Cr}^{3+}$ is very attractive for this application. In this section we discuss the white light generation obtained by using this nanophosphor impregnated with a Coumarin 480 blue dye. The emission spectra of sample N1 impregnated with a Coumarin(mg)/absolute ethanol(ml.) ratio of 0.6/20 (Sample C1) and with a 1/20 ratio (Sample C2) under 340 nm excitation are shown in figure 4.9a. The CIE coordinates were (0.30,0.36) for sample C1, very near to the ideal coordinates (0.33,0.33) for white light, see figure 4.9b.

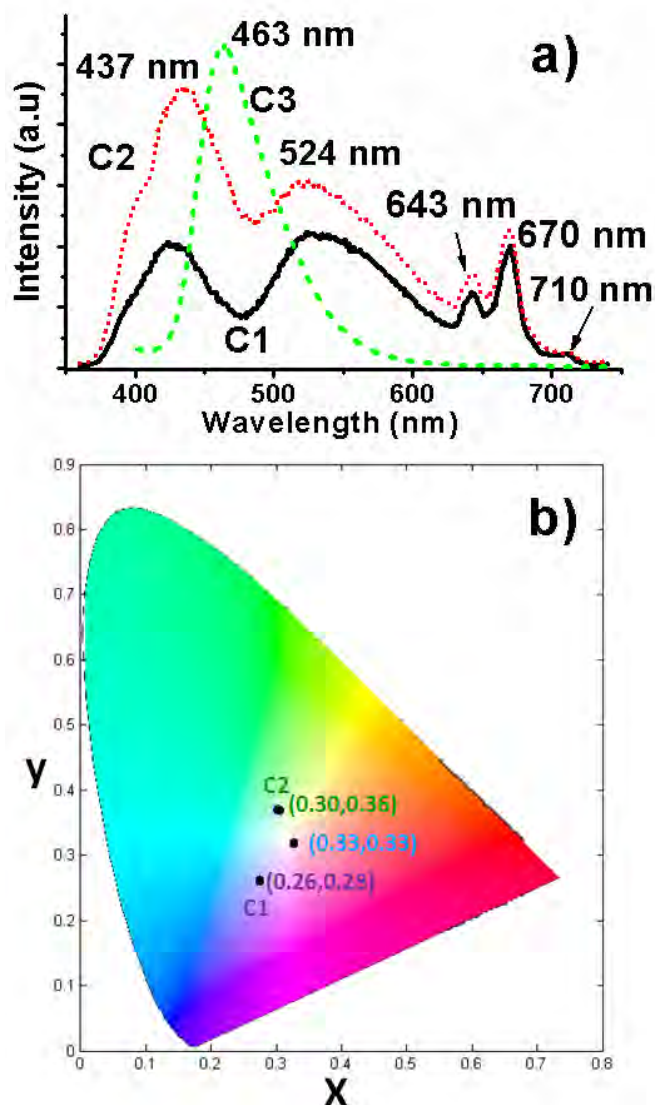


Figure 4.9: a) Photoluminescence spectra under 340 nm excitation of samples C1 (0.6 mg), C2 (1 mg) and Coumarin 480 (0.6 mg). b) CIE coordinates of C1 and C2 samples.

The CIE coordinate of sample C2 was (0.26,0.28), slightly shifted to the blue region as a result of the dominant blue peak centered at 437 nm, therefore the emission observed by the naked-eye was bluish-white. The fluorescence spectrum of Coumarin presented an emission peak at 463 nm when it is dissolved in absolute ethanol (sample C3), but it has a shifting of 26 nm to shorter wavelengths when it is impregnating the YAG/YAM nanophosphor. Such displacement in the emission peak from 463 nm to 437 nm is associated partly to

the interaction of the Coumarin dye with the nanophosphor and partly is the blue absorption effect of Ce^{3+} and Pr^{3+} . Furthermore, the three components in the system are excited simultaneously, therefore the emission of Pr^{3+} decreases in C1 in comparison to N1, since the excitation wavelength would be absorbed by three elements (Ce^{3+} , Cr^{3+} and Coumarin). Nevertheless, the emission of Ce^{3+} in C1 increases with respect to N1, suggesting that Ce^{3+} reabsorbs the emission at 463 nm from Coumarin. This confirms the shifting in the emission peaks of C1 compared to N1 produced by the reabsorption of Ce^{3+} .

In this particular system, only the blue emission could be controlled since the YAG/YAM: Ce^{3+} , Pr^{3+} , Cr^{3+} nanophosphors had a fixed concentration of 0.1 mol% for the Ce^{3+} and Pr^{3+} . Nevertheless, it is also possible to change the concentration of Ce^{3+} and Pr^{3+} to have better control of the CIE color coordinates. In this way, this system could be employed to create warm and cool white light sources by tailoring the concentrations of Ce^{3+} , Pr^{3+} and the blue dye. Furthermore, it is necessary to find a replacement material for Coumarin since this colorant is bleached after prolonged exposure to UV excitation. Such material should provide good emission efficiency around 460 nm in order to improve the white light emission. The solution of all those problems is the objective of a current work that will be reported elsewhere.

4.5 Hybrid LEDs made with YAG: Ce^{3+} nanophosphors

The YAG phosphors (synthesized as reported in ref. 25) were used in combination with a blue polymer light emitting diode (PLED) to generate white light. Figure 4.10 presents the emission and excitation spectra of cerium doped YAG nanophosphors. The YAG: Ce^{3+} nanophosphors had an maximum emission peak at 530 nm and its maximum of excitation is achieved at 460 nm. This figure also presents the electroluminescence spectrum from the blue emitting OLED made with poly[(9,9-dioctylfluorenyl-2,7-diyl)-co-(4,4'-(N-(4-sec-butylphenyl)) diphenylamine)] (TFB), see blue dashed curve. The main emission band of TFB

is overlapping the excitation spectrum of the YAG nanophosphor as observed in figure 4.10, then, it is expected to get white light due to the combination of the blue light coming from the OLED and the green-yellow light coming from the YAG:Ce³⁺ nanophosphors.

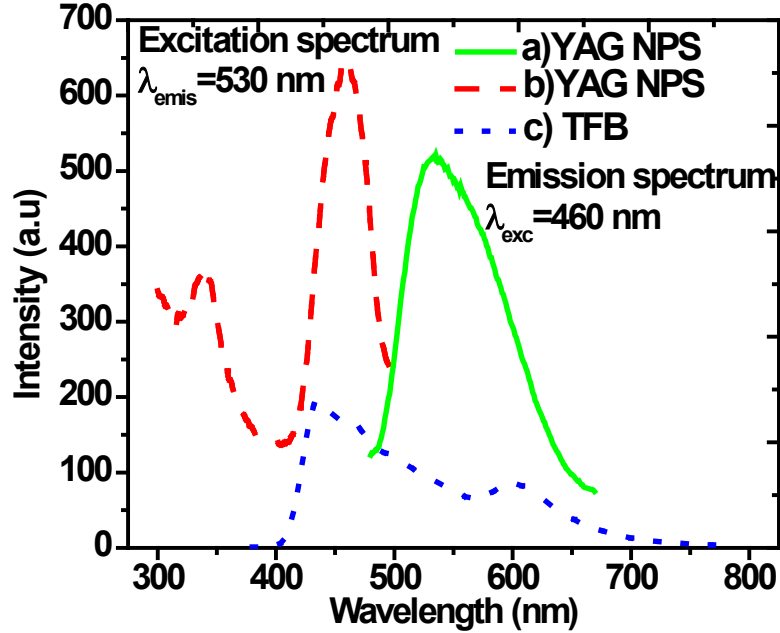


Figure 4.10: a) and b) are the excitation and emission spectra of the doped YAG nanophosphors, c) is the electroluminescence spectra of the OLED made with TFB exclusively.

The blue emitting device was fabricated using the method of spin coating, the configuration for this was: a) ITO/PEDOT (40 nm)/ TFB (60 nm)/Cs₂CO₃/Al (100 nm) with an effective emitting area of 3 mm x 3mm (device 2). The poly(3,4-ethylenedioxythiophene) poly(styrenesulfonate) (PEDOT:PSS) acts as a hole transport material and TFB as the blue emitter. After the deposition of the organic layers, a film of YAG:Ce³⁺ nanophosphors (2 μ m) was deposited by spin coating on the glass side of the blue PLED. Another identical blue LED device but without the phosphor layer was made to be used as a reference, it will be referred as “device 1” while the device with the phosphor will be called “device 2”.

Figure 4.11 shows the normalized emission spectrum of the YAG:Ce³⁺ nanophosphors (photoluminescence, green curve), TFB (electroluminescence, blue curve) and the overlapped emission of the blue PLED and the cerium doped YAG nanophosphors (photo and electroluminescence, red curve).

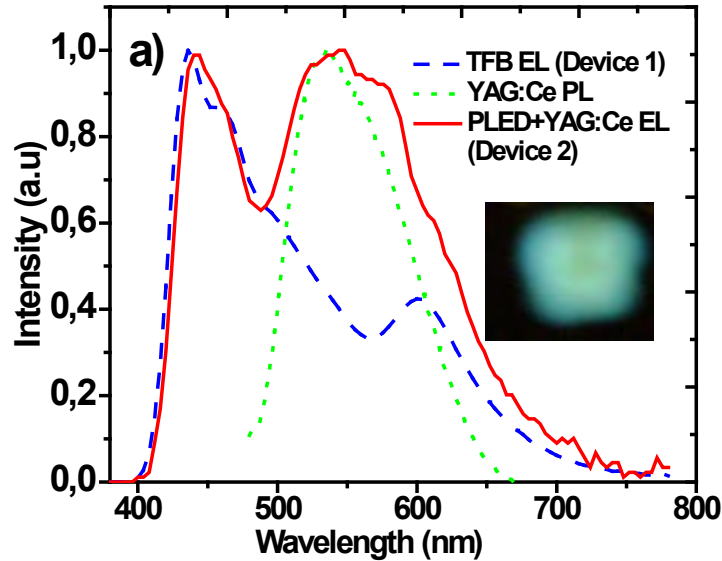


Figure 4.11: a) Emission spectra of the YAG:Ce³⁺ nanophosphors, b) electroluminescence from TFB and c) emission of the hybrid device (blue PLED+ YAG:Ce³⁺).

As expected, the emission spectrum corresponding to the combination PLED+YA:Ce³⁺ is broad, suggesting that overlapping of the emissions coming from the PLED and the YAG:Ce³⁺ was achieved successfully. The inset in figure 4.11 shows the white light emission generated in this system and the corresponding CIE coordinate is (0.31, 0.35), which is close of the ideal white light with CIE coordinates of (0.33, 0.33).

Figure 4.12 shows the voltage vs. current (I-V curve) curves for devices 1 and 2 (see blue and green curves), the turn on voltage for both devices was 4V. As expected, the I-V curve for devices 1 and 2 is almost the same, since they were made under the same conditions of fabrication. The only difference between them is the brightness of the combined emission due to the presence of the

YAG:Ce³⁺ nanoparticles. The maximum brightness were 2600 Cd/m² (at 10V) and 266 Cd/m² (at 9V) for device 1 and 2 respectively, see figure 4.12. The decrease by a factor of 10 of the electroluminescence in device 2 compared to device 1 is mainly due to the poor absorption of YAG nanophosphors, scattering of light through the inorganic film and the waveguiding effect produced by the substrate of ITO. The inset in Figure 4.12 shows the general configuration of the hybrid device. The recombination of electrons coming from the Al and the holes coming from the ITO is carried out in the TFB polymer to produce blue light. The energy barrier height to inject electrons from the Al to the LUMO of TFB is high (2.2 eV). Therefore, Cs₂CO₃ is introduced to improve the confinement of electrons in the layer of TFB resulting in a good balance between electrons and holes injected. It is worthy to notice that the efficiencies for devices 1 and 2 at an operation voltage of 9V were 0.39 Cd/A and 0.06 Cd/A, the reduction in efficiency was just 84% in device 2 with respect to device 1. It is believed that an increase in efficiency is possible by increasing the brightness of the blue PLED at lower voltages and by increasing the absorption efficiency of YAG:Ce³⁺ nanoparticles. The increase in absorption could be made by increasing the concentration of Ce³⁺ in the YAG host.

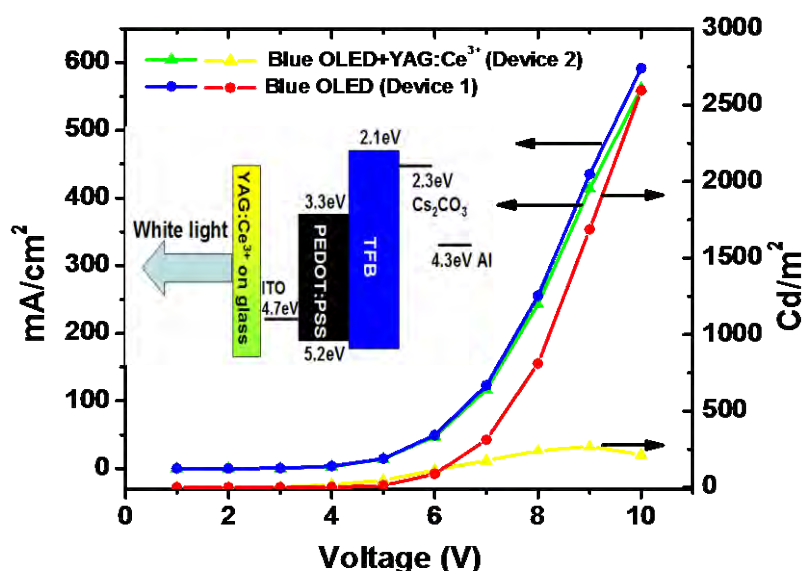


Figure 4.12: I-V curve for the hybrid OLED (curves green and blue) Luminance vs. voltage (red and yellow curves). The inset is the band diagram for this device.

4.6 Conclusions for chapter 4

Codoped YAG/YAM:Ce³⁺,Pr³⁺,Cr³⁺ nanopowder with an average crystallite size of 50 nm was prepared by the precipitation method. The phase composition is strongly dependent on the component used for preparation and annealing temperature. 55 wt% of YAG crystalline phase was observed for samples annealed at 900 °C and increased to 65 wt% with the introduction of ammonia. Furthermore, the increase of annealing temperature up to 1100 °C stabilizes 100% the YAG crystalline phase with and without the presence of ammonia. However, such annealing temperature enhances the formation of Ce⁴⁺, Pr⁴⁺ and color centers induced by the charge compensation. A broad red emission band overlapped to Ce³⁺ emission was produced under 340 nm excitation due to the presence of trace impurities of Cr³⁺, this broad green-yellow-red emission band produced by the Ce³⁺, Pr³⁺ and Cr³⁺ ions was used along with a blue dye to

produce white light, this system had CIE coordinates (0.30, 0.36) which is close to ideal white. This demonstrates that the phosphor synthesized here is good candidate to produce white light by combining the broad red emission of Pr^{3+} and Cr^{3+} with the blue emission from some organic or inorganic material.

A hybrid white emitting LED with YAG:Ce^{3+} phosphors was developed, it has a turn on voltage of 4V and a maximum luminance of 266 Cd/m^2 at 9V. The CIE coordinate for this device was (0.31, 0.35) which is near of the ideal coordinate of (0.33, 0.33).

References chapter 4

- [1] A. C. Larson and R. B. Von Dreele, Los Alamos National Laboratory Report No. LAUR, 86–748 (2000)
- [2] Paul Erhart Appl. Phys. 111, 113502 (2012)
- [3] H. S. Jang, W. B. Im, D. C. Lee, D. Y. Jeon, and S. S. Kim, J. of Lumin. 126, 371 (2007).
- [4] Y. Sanga, H. Liua, Y. Lva, J. Wanga, T. Chena, D. Liua, X. Zhanga, H. Qina, X. Wanga, and R. I. Boughton, J. of Alloys and Comp. 490, 459 (2010)
- [5] D. Li and Richard B. Kaner J. AM. CHEM. SOC. 128, 968 (2006)
- [6] Y. Zhang, and H. Yu, Ceramics International 35, 2077 (2009).
- [7] J. Wang, W. Miao, Y. Li, H. Yao, and Z. Li, Materials Letters 63, 1794 (2009).
- [8] R. Srinivasan, R. Yogamalar, and A rumugam Chandra Bose, Advanced Science Letters 2, 65 (2009).
- [9] Hsuan-Min Lee, Chao-Chi Cheng, Chi-Yuen Huang, Materials Research Bulletin 44, 1081 (2009)
- [10] Y. Pan, M. Wu, and Q. Su, J. of Phys. and Chem. of Solids 65, 845 (2004).
- [11] H. Yang, and Y. S. Kim, J. of Lumin. 128, 1570 (2008).
- [12] D. Pawlak, Z. Frukacz, Z. Mierczyk, A. Suchocki, and J. Zachara, Journal of Alloys and Compounds 275, 361 (1998).
- [13] A. P. Vink, P. Dorenbos, J. T. M de Haas, H. Donker, P. A. Rodnyi, A. G. Avanesov and C. W. E van Eijk, J. Phys.: Condens. Matter 14, 8889 (2002).

- [14] N. A. Ivanov, V. D. Lokhnygin, A. A. Fomichev, V. M. Khulugurov, and B. P. Chernyago, J. of appl. Spectros. 46, 207 (1987).
- [15] Q. Zhang, T. Liu, J. Chen, and X. Feng, Physical review B. Condensed matter and materials physics 68, 064101 (2003).
- [16] S. Chawla, T. Roy, Kanishka Majumder and Ashish Yadav, J. of Exper. Nanosci. 1 (2012)
- [17] P. Boutinaud, R. Mahiou, E. Cavalli and M. Bettinelli, J. Alloys Compounds 122-123, 430 (2007).
- [18] P.J. Deren, R. Pazik, W. Strek Ph. Boutinaud and R. Mahiou, J. Alloys and Compounds, 451, 595 (2008).
- [19] E. van der Kolka, P. Dorenbos, C.W.E. van Eijk, A.P. Vink, C. Fouassier and F. Guillen, J. Lumin. 97,212 (2002).
- [20] S. Zhou, Z. Fu, J. Zhang, S. Zhang, J. Lumin. 118, 179 (2006).
- [21] S. R. Jeon, M. Gherasimova, Z. Ren, J. Su, G. Cui, J. Han, H. Peng, Y. K. Song, A. V. Nurmikko, L. Zhou, W. Goetz and M. Krames, Jpn. J. Appl. Phys. 43, L1409 (2004).
- [22] K. Davitt, Y. K. Song, W. R. Patterson III, and A. V. Nurmikko, Optics Express 13, 9548 (2005).
- [23] H. Peng, E. Makarona, Y. He, Y. K. Song and A. V. Nurmikko, Appl. Phys. Lett. 85, 1436 (2004).
- [24] J. S. Cabalu, A. Bhattacharyya, C. Thomidis, I. Friel, and T. D. Moustakasa, J. of Appl. Phys. 100, 104506 (2006).

[25] R. Ovalle, A. Arredondo, L. A. Diaz-Torres, P. Salas, C. Angeles, R A. Rodríguez, M. A. Meneses and E. De la Rosa, Proceeding SPIE 2, 5530-5539 (2004)

Chapter 5

5.0 Conclusions

The synthesis, characterization, optical properties of ZnO nanoparticles and YAG/YAM:Ce³⁺,Pr³⁺,Cr³⁺ nanophosphors, as well as their use in the fabrication of hybrid LEDs were presented. In the case of the ZnO nanoparticles, it was possible to tune the morphology of ZnO quantum dots according to the surfactant used during its synthesis. By using the surfactant TEA, ZnO quantum dots with a size of 5 nm in average were obtained and those nanoparticles presented strong blue emission, its quantum yield was 81%, which is the highest reported to date to the best of our knowledge. In addition, yellow emission was obtained when the temperature of synthesis was changed. The origin and mechanisms of emission of the ZnO were studied and it was concluded that the blue emission came from Zinc interstitials and the yellow emission from oxygen vacancies. If DCA is used as surfactant, ZnO nanorods are obtained and the fluorescence generated from those nanoparticles is white light. Those nanorods were used in ZnO based LEDs (hybrid device) which had a turn on voltage of 6V and low current consumption. The white light generated in those hybrid LEDs is tunable from cool white light to warm white light, but the brightness is poor. To improve the efficiency, it is required to introduce electron transport layers, in this way the balance of injected holes and electrons could be better and it is expected stronger emission of white light. It was possible to tune from cool to warm white light in photoluminescence or in electroluminescence when those nanoparticles are used in hybrid LEDs.

In the case of YAG/YAM:Ce³⁺,Pr³⁺,Cr³⁺ nanophosphors, it is demonstrated that a broad red emission can be incorporated to the cerium emission by exciting at 340 nm. This red emission has been scarcely reported in YAG. By using the blue

Coumarin dye, it was possible to get white photoluminescence with CIE coordinates of (0.30, 0.36). In addition, a blue PLED was fabricated and we incorporated YAG:Ce³⁺ nanophosphors on the glass side of it in such a way that the blue emission coming from the PLED excited this phosphor and the combination of the transmitted blue light and the green-yellow emission coming from the cerium doped YAG produced white light with CIE coordinates of (0.31, 0.35). This device had a maximum brightness of 266 Cd/m² at 9V. It is necessary to control the thickness of the YAG:Ce³⁺ layer to have better brightness. All the CIE coordinates obtained in photoluminescence or electroluminescence in this work of thesis are near of the ideal coordinates of white light (0.33, 0.33), indicating that the ZnO or the YAG/YAM phosphors could be useful for applications in lighting or displays. Nevertheless, more work is needed to optimize the hybrid devices and to be commercially competitive.